October 2015
Volume 121
Issue 1954
£5.20

www.electronicsworld.co.uk

Electronics WORLD

THE ESSENTIAL ELECTRONICS ENGINEERING MAGAZINE

SPECIAL REPORT ON COMMUNICATIONS:

- Antenna design
- RF and microwave filters
- RFID

Applying **Modern Machine Vision** Technologies to Security

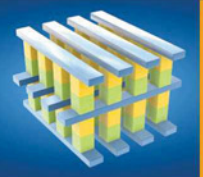

Technology
First new memory category since NAND flash in 1989

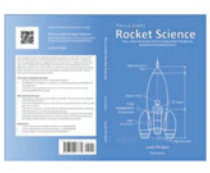

Book Giveaway
'This is (not) Rocket Science' by Lucio di Jasio

Products
Latest connectors, power meters and enclosures

The World's Largest Selection of Electronic Components Available for Immediate Shipment!™

We Source What's Inside YOUR DESIGN

FREE SHIPPING ON ORDERS OVER £50!*

0800 587 0991 • 0800 904 7786

DIGIKEY.CO.UK

Digi-Key® ELECTRONICS

1,100,000+ PRODUCTS IN STOCK | 650+ INDUSTRY-LEADING SUPPLIERS | 100% AUTHORIZED DISTRIBUTOR

*A shipping charge of £12.00 will be billed on all orders of less than £50.00. All orders are shipped via UPS for delivery within 1-3 days (dependent on final destination). No handling fees. All prices are in British pound sterling and include duties. If excessive weight or unique circumstances require deviation from this charge, customers will be contacted prior to shipping order. Digi-Key is an authorized distributor for all supplier partners. New product added daily.

ecia MEMBER ecsn member CEDA

Cover supplied by MOUSER ELECTRONICS
More on pages 12-14

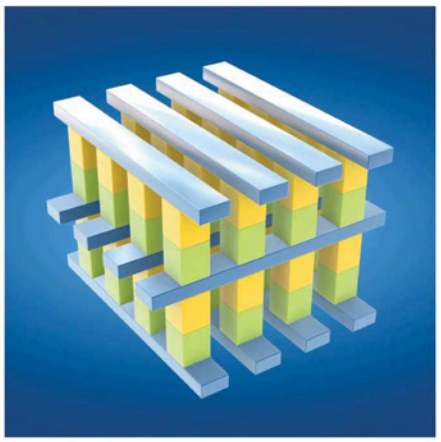

06

REGULARS

36

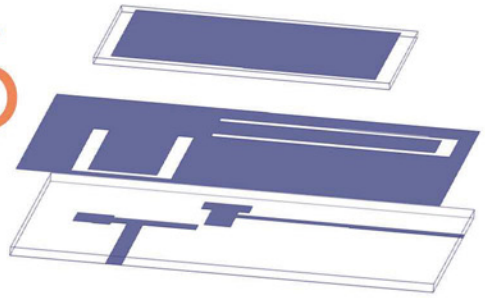

44

FEATURES

Working at the cutting edge of technology

Signal generation, analysis and phase noise test for demanding requirements

When working at the cutting edge of technology, you shouldn´t waste your time with inferior tools. Rely on measuring instruments evolved in the spirit of innovation and based on industry-leading expertise.

Instruments like the R&S®SMW200A vector signal generator, the R&S®FSW signal and spectrum analyzer and the R&S®FSWP phase noise tester. Each is at the crest of today´s possibilities.

See for yourself at
www.rohde-schwarz.com/ad/highend

ROHDE&SCHWARZ

POWERING INDUSTRIAL SYSTEMS

Designing power supplies for industrial systems is becoming increasingly complex. Designs are moving to advanced FPGAs, ASICs, processors and memories, and the number of voltage rails continues to grow. The industrial market is a hotbed for medium-sized companies that are functional experts, but do not typically have in-house power design expertise.

With applications adding more intelligence whilst complying with green energy standards, IC suppliers have to deliver solutions that meet these power needs, yet are straightforward to use. Power management system development must be reliable and address the challenges of a noisy industrial environment, including 15-25% power surges that can cause spikes of up to 60V on a 48V distribution bus.

This is why many designers turn to power modules, which typically operate as self-contained power management systems, and include all the major components such as the PWM controller, FETs, inductors and compensation circuitry; only the input and output capacitors are needed to create an entire power supply.

Power modules have been around a while, but they sometimes required performance compromise as a tradeoff for their simplicity. Now, modules leverage semiconductor packaging technology and innovative design techniques allowing them to deliver the level of unprecedented power density and performance required by even the most rigorous applications, whilst being very easy to use; no longer needed are clunky discrete solutions with expensive heat sinks and fans taking up valuable board space and adding risk to the system.

Another trend we see is customers moving to a higher-voltage distribution bus. Traditionally, designers have been stepping down from a 42V or 36V bus to a 12V or even 8V intermediate bus, and then directly stepping down to the point-of-load (POL). However, those designers using a higher voltage system bus now want to eliminate the intermediate bus and convert directly from 48V down to POL. Recently this became possible with the introduction of a 60V synchronous buck controller featuring the industry's lowest duty cycle. This enables the direct step-down conversion from 48V to a 1V POL.

> Designers using a higher voltage system bus now want to eliminate the intermediate bus and convert directly from 48V down to POL

Eliminating the DC-DC converter saves cost, improves reliability and is 2-3% more efficient. And, a bonus is the lower power loss on the system bus – another benefit from bussing around a lower input current at higher voltage.

The theme that should be coming across is the need to simplify power system design without compromising performance to help equipment makers meet their design goals cost-effectively. Suppliers need to look at every element of power system design to identify where innovation will help most. For example, today's switching regulators and controllers typically require customers to build a compensation network by selecting external resistors (R_s) and capacitors (C_s) to stabilize the control loop. This is time-consuming and requires a lot of trial and error with different R and C combinations to get the design stable under all operating conditions. Integrating internal compensation into switching regulators, power modules and controllers has eliminated this time consuming step for our customers.

I've been a part of power management IC development for many years, and this decade is proving to be one of the most exciting. Industrial applications are evolving more quickly and in more interesting ways with the advent of smart factories, always-on connected devices and highly dense computing capability. The simultaneous need to reduce power consumption has created an environment ripe for innovation in power management. It is satisfying to see the latest generation of power solutions address not only the advanced power needs but do it in a way that addresses the resource constraints on our customers' design teams.

By Mark Downing, Senior Vice President for Strategy and Infrastructure Power Products at Intersil (www.intersil.com)

EDITOR:
Svetlana Josifovska
Tel: +44 (0)1732 883392
Email: svetlanaj@sjpbusinessmedia.com

SALES:
James Corner
Tel: +44 (0)20 7933 8999
Email: jamesc@electronicsworld.co.uk

Philip Woolley
Tel: +44 (0)20 7933 8989
Email: philipw@sjpbusinessmedia.com

DESIGN: Tania King

PUBLISHER: Justyn Gidley

ISSN: 1365-4675

PRINTER: Buxton Press Ltd

SUBSCRIPTIONS:
Subscription rates:
1 year: £62 (UK);
£89 (worldwide)
Tel/Fax +44 (0)1635 879361/868594
Email: electronicsworld@circdata.com

2nd Floor,
52-54 Gracechurch Street,
London, EC3V 0EH

Follow us on Twitter
@electrowo

Join us on LinkedIn

INTEL AND MICRON CREATE A NEW CLASS OF SUPER MEMORY

Intel and Micron Technology unveiled 3D XPoint, a non-volatile memory that promises to revolutionize any device, application or service that needs fast access to large data sets. This is the first new memory category since the NAND flash first appeared in 1989.

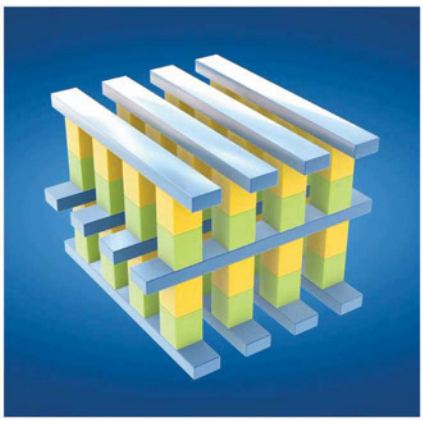

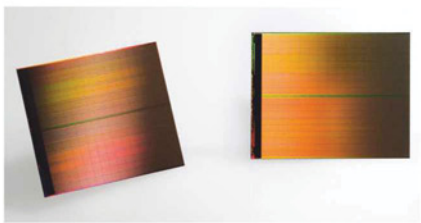

Intel and Micron invented unique material compounds and a crosspoint architecture (above) for a memory technology (below) that is ten times denser than conventional memory

3D XPoint's innovative, transistorless, crosspoint architecture creates a three-dimensional checkerboard where memory cells sit at the intersection of word lines and bit lines, allowing cells to be addressed individually. As a result, data can be written and read in small packets, leading to faster and more efficient read/write processes.

Perpendicular conductors connect 128 billion densely-packed memory cells. Each memory cell stores a single bit of data, and can be written to or read by varying the amount of voltage sent to each selector, eliminating the need for transistors and increasing capacity.

With a small size, fast switching selector, low-latency crosspoint array and a fast write algorithm, the cell is able to switch states faster than any other non-volatile memory currently in use.

In addition to the tight crosspoint array structure, memory cells are stacked in multiple layers. The initial technology stores 128Gb per die across two memory layers. Future generations, however, will have an even greater number of memory layers for improved system capacities.

As the digital world quickly grows – from 4.4 zettabytes of digital data created in 2013 to an expected 44 zettabytes by 2020 – it is expected 3D XPoint to play a key role in turning this immense amount of data into valuable information in nanoseconds.

The non-volatile nature of the technology also makes it great choice for a variety of low-latency storage applications, whereas the compact structure results in high density and high performance.

One of the most significant hurdles in modern computing is the time it takes the processor to reach data in long-term storage. 3D XPoint is expected to change that as it is up to 1,000 times faster, ten times denser and with 1,000 times greater endurance than NAND memory.

"For decades, the industry has searched for ways to reduce lag time between processor and data to allow much faster analysis," said Rob Crooke, senior vice president of Intel's Non-Volatile Memory Solutions Group.

"This new class of non-volatile memory achieves this goal and brings game-changing performance to memory and storage solutions."

UK TECH PROFESSIONALS ARE CONSIDERING INTERNATIONAL JOB OPPORTUNITIES

The attraction of international assignments for UK-based tech professionals is growing stronger, with 72% surveyed indicating they would consider an international move if the right opportunity came along, states research conducted by UK consultancy Dice.

British professionals would gladly move to the US, Australia and Canada for the right job as they find these top-three countries offer better career opportunities and work/life balance. Other countries of interest are France, Germany, New Zealand, Spain, United Arab Emirates, India, Italy, the Netherlands, Scandinavia and Saudi Arabia.

Some 41% of respondents cited lifestyle-related factors as the primary reason for contemplating a move abroad rather than financial gains.

And, it is not just overseas positions that are being considered; some 69% are happy to move within the UK for the right job. London was attractive for the increased earnings potential, whereas the South West for lifestyle-related factors. Similarly, quality-of-life, career advancement and family considerations all ranked ahead of increased earnings for those respondents considering a move to Scotland.

"Tech professionals fully recognise the highly transferable nature of their skills. As a result, they are often more open than other professionals to the concept of moving – to improve their career or their lifestyle. This dynamic, in turn, places greater pressure on employers to ensure they have the right culture and working environment in which tech professionals will thrive. Those businesses with an international footprint should also actively facilitate mobility within the organization in order to both attract and retain strong tech talent," said Jamie Bowler, Dice's Marketing Director for UK and Europe.

Nearly a quarter (23%) of respondents are actively looking to make a move abroad, with 24% already on the lookout for new positions within the UK.

Make No Compromises

Increase Your Design's Functionality with 8-bit PIC® MCUs

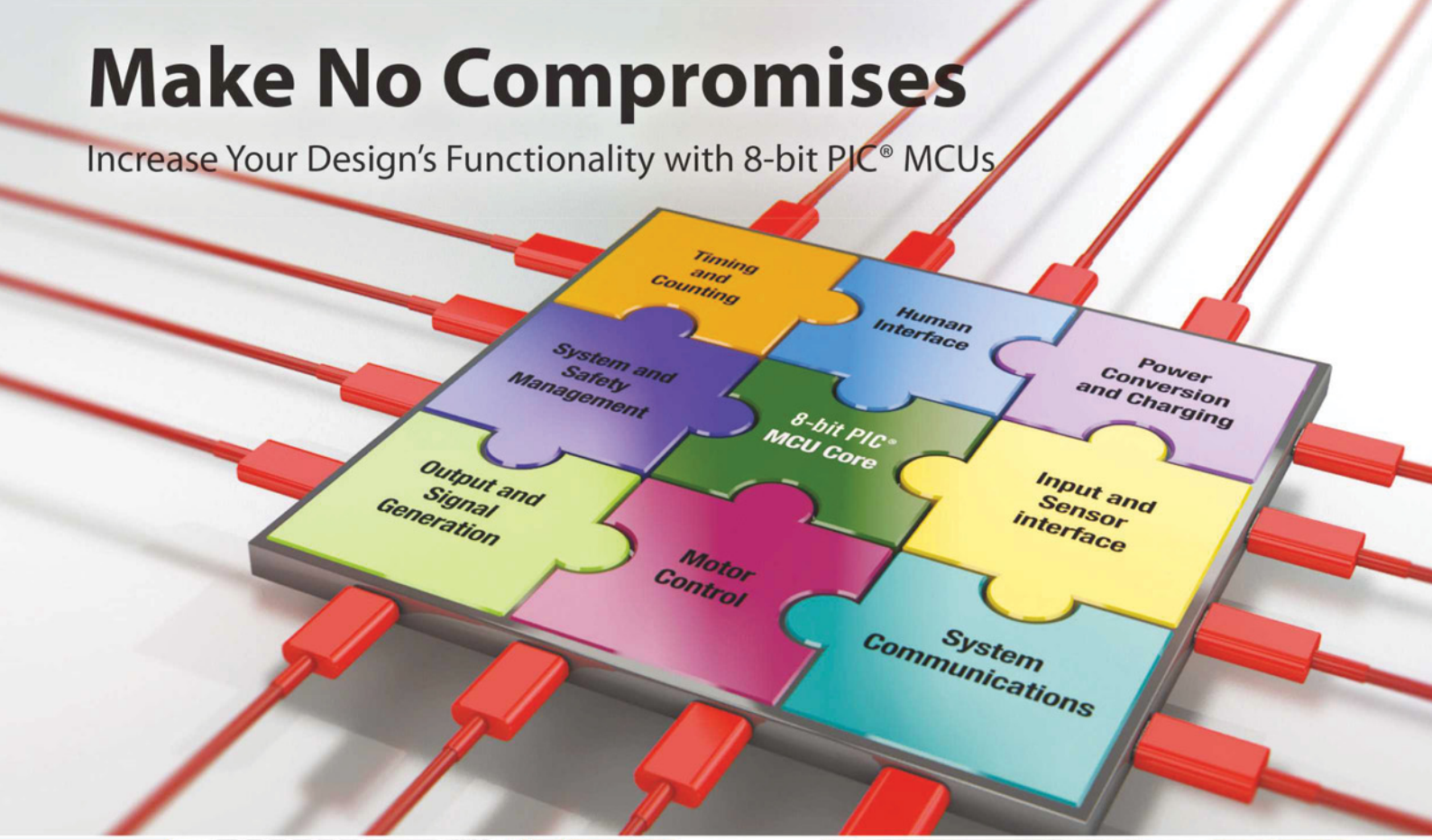

In embedded system design, reality demands that compromises are made at every phase. Tradeoffs between performance, functionality and cost often prevent you from bringing your best ideas to market. We believe there's a better way. That's why we've architected our latest 8-bit PIC® microcontrollers (MCUs) with flexible, "core independent" blocks of hardware intelligence that react quickly, consume very little power and are much more code-efficient than a software-based approach. In essence, Core Independent Peripherals help you easily combine many complex system functions onto a single MCU, increasing speed and flexibility, while reducing power consumption and cost. Design with 8-bit PIC MCUs, and you won't have to compromise.

Enable system functions with:

- Maximum flexibility
- Minimum latency
- Reduced cost

FLEXIBLE INTELLIGENCE MADE EASY

8-BIT PIC® MICROCONTROLLERS

microchip DIRECT
www.microchipdirect.com

MICROCHIP

www.microchip.com/8-bit

THIS SERIES PRESENTS THE RASPBERRY PI SINGLE-BOARD COMPUTER, ITS FEATURES AND BENEFITS, AND ITS USE IN VARIOUS PROJECTS

Webcam And Computer Vision

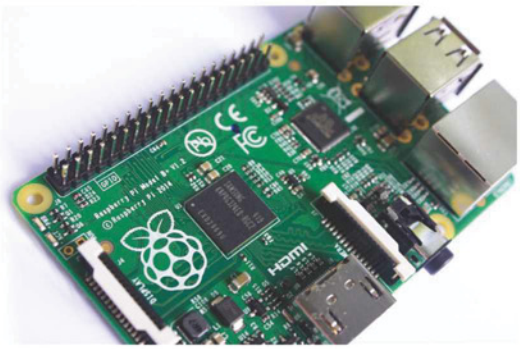

BY **MIKE COOK, JONATHAN EVANS** AND **BROCK CRAFT**

Raspberry Pi vision can be set up using a webcam or the Pi camera module. With image-processing techniques, the Raspberry Pi can analyze images to identify motion, colours and shapes.

A webcam can be plugged into Raspberry Pi's USB port or an attached USB hub. We strongly recommend using a powered USB hub for the webcam because the Raspberry Pi can't support much more than a keyboard and a mouse on its own power supply. Compatibility between the webcam and the Raspberry Pi can be checked at www.elinux.org/RPi_USB_Webcam.

Once the webcam is connected and powered up, type the following commands to see if it comes up on the Raspberry Pi listing:

$ lsusb

$ ls /dev

There should be two listings. We used a Creative Technology webcam; in the second listing, look for video0. If you see both, you know your webcam is working. If not, shut down the Raspberry Pi, unplug the webcam and start the process again.

If you have a Raspberry Pi camera module, make sure it's connected and the camera module setting is switched on. Test it by typing one of the commands below, and pressing 'enter': you should have a wonderful portrait of yourself saved to a file called test.bmp.

Taking A Picture With A Webcam

To take a picture with a webcam, use the following command:

fswebcam -d /dev/video0 -q -r 1024x768 test.bmp

fswebcam is a utility that's included in the Raspbian image. Take a close look at the command to understand what each part does. The -d option is the device name. (Earlier, you looked for the video0 file in the /dev directory.)

The -q option is a quiet option that does not display any text to the screen during operation. The -r option sets the resolution to 1,024 pixels wide by 768 pixels high.

For a full list of options, go to the –help option, and all of them will be written to the screen:

$ fswebcam –help

Taking A Picture With The Raspberry Pi

To take a picture with the Raspberry Pi camera module, use this command:

raspistill -o test.bmp -t 1 -w 1024 -h 768 -e bmp

raspistill is a utility written specifically for the Raspberry Pi camera. The -o is for output, followed by the file name where we want the picture to be stored (test.bmp). -t is how many seconds it waits before taking a picture (the default is 5 seconds). As you might have guessed, -w is the width and -h the height of the picture.

As before, for a full list of options, pass the –help option, and all them will show up on screen:

$ raspistill –help

Viewing Pictures

Viewing pictures on the Raspberry Pi is best done through x, as follows:

$ startx

Double-clicking the lxTerminal icon on the desktop and entering this command will show the picture:

$qinv -f test.bmp

qinv is a utility that displays images. If it isn't installed, you can type the following command to install it:

$ sudo apt-get install qiv ●

RASPBERRY PI PROJECTS FOR DUMMIES

This column is an edited extract from 'Raspberry Pi Projects For Dummies' by Mike Cook, Jonathan Evans and Brock Craft (ISBN: 9781118766699), published by Wiley.

If you want a copy of the book, enter our giveaway by sending an email to the Editor at svetlanaj@sjpbusinessmedia.com, with the book's title in the subject field.

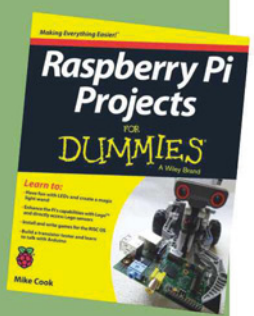

BEHIND EVERY GENUINE PART

THERE'S A DISTRIBUTOR YOU CAN COUNT ON

By partnering with 2,500 brands you know and trust, we make thousands of the latest products available to you every month. With our well-stocked range of electronics, automation and control, and tools and consumables, you can count on us for all the parts you need.

uk.rs-online.com

RS

PIM Requirements Must Increase To Support Evolving DAS Systems

BY **LUIGI TARLAZZI**

Several years ago, passive intermodulation (PIM) was a virtually unknown performance metric in distributed antenna systems (DAS); today it is increasingly recognized as one of the most critical requirements for optimum system performance. Hypersensitive antennas and radios, multiple frequency overlays and more components in the RF path create an environment in which the margin for error regarding PIM continues to shrink. Given the high susceptibility of current DAS systems, even small levels of PIM distortion can significantly impact network performance, as measured by upload speed.

Outdoor macro sites were the first deployment scenarios in which PIM issues had to be tackled. High power levels from the base transceiver station (BTS) ports and a more complex RF paths to the antennas – including jumpers, filters and tower mounted amplifiers (TMAs) – contribute to generating PIM that can be detrimental to the quality of wireless service. Due to the limited uplink (UL) transmit power of mobile terminals, the uplink receive sensitivity is a critical parameter to optimize outdoor scenarios for a balanced downlink/uplink path loss.

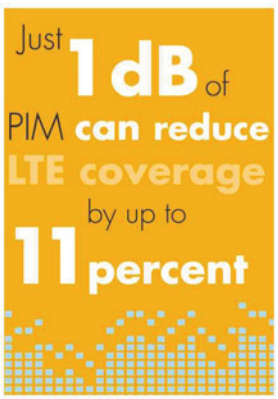

High and reliable data throughput values are even more important in DAS environments, such as stadiums, where there are many components in the RF path that can contribute to PIM generation. The minimum PIM specification for every component is improving continually. PIM specifications for RF components (splitters, couplers, etc) and antennas have transitioned from -140dBc to -150dBc and are now moving to -153dBc and -160dBc. With the passive components (splitters, hybrid couplers and directional couplers, etc) located closer to the signal sources in these systems, it is critical that the PIM specification for these devices is at the highest levels.

Passive components used in RF signal distribution networks have wideband frequency support. Therefore, multiband and multicarrier signals from DAS remote unit output ports can mix together at every passive stage and generate a large variety of detrimental PIM products falling in multiple uplink bands. For this reason, PIM requirements for these passive components must be more stringent.

Major Performance Threats

There are a number of issues to consider when evaluating PIM requirements for RF components in the passive distribution network of a multi-operator/multiband DAS installation:

- The number of frequency bands and amount of spectrum used in each band are increasing, creating new and additional mixing products, and generating wider bandwidths of PIM.
- When multiple carriers on the same DAS infrastructure share a given band and are evenly spaced, the severity of the PIM products within the shared frequencies can multiply.
- DAS systems are built using multiple cables and passive components in a cascaded architecture. The PIM performance is important for each element, but the passive components will be closer to the RF source – especially at high transmit (TX) power levels – and will have a greater influence on the overall PIM level produced.
- PIM produced in the cabling and connector network may degrade over time, so using high-PIM-rated devices is critical for long-term operation of the system.

All these issues represent major threats to the performance of DAS installations, which must support high data rates, using large channel counts and multiple-in/multiple-out (MIMO) antenna schemes. This is an environment where PIM will have a tremendous impact on system performance, due to potential PIM creation through the multitude of channels and the need for minimum signal-to-interference noise ratio (SINR) for optimum MIMO performance.

Additional PIM Challenges

For wireless technologies like LTE, with one-to-one frequency reuse, intercell interference is another key challenge. It's critical to

minimize the UL transmission power of mobile devices at the cell edge, to reduce interference to adjacent cells. As the UL noise floor – as recognized by the BTS – rises, the mobile device boosts its UL transmission power to minimize SINR at the BTS receiver. As more interference is created, the cell begins to shrink due to the increasing noise at the receiver.

> Passive components used in RF signal distribution networks such as distributed antenna systems (DAS) can contribute to the generation of passive intermodulation (PIM)

MIMO technology is part of the toolkit mobile operators are using to tackle the ever-increasing demand for mobile data capacity. It has been largely demonstrated that the multiplexing of independent data-streams can be supported only in good RF channel conditions. That poses severe constraints on the coverage levels required as well as the signal quality, given that the SINR has become a key performance indicator to optimize.

Furthermore, LTE-Advanced supports MIMO schemes for the uplink path as well. As a result, the SINR requirements must be met even at the BTS receiver, which makes it even more critical to limit the uplink noise rise.

Carrier aggregation (CA) is another key feature introduced by LTE-Advanced. Wireless operators will combine different frequency bands to cope with spectrum fragmentation. For a DAS installation, assuming both intra- and inter-band CA schemes with more and more downlink (DL) component carriers aggregated to boost DL data rate, the number of possible multicarrier combinations can get extremely high, with a consequent higher probability of generated PIM products falling in uplink bands.

All these can make PIM issues on modern DAS systems targeted for LTE and LTE-Advanced technologies even more detrimental than for legacy networks.

To adequately protect their investment in DAS infrastructure over the long term, operators must begin to deploy network components that provide increasingly higher PIM margins. This involves transitioning from the current devices (PIM rated up to -153dBc) to passive devices that are both certified and can be verified for PIM performance of -160dBc. Going forward, these higher-performing passive components with a PIM rating of -160dBc will play a crucial role in the long-term success of high-end DAS solutions. ●

Luigi Tarlazzi is Embedded Product Line Manager for the Americas at CommScope's Distributed Coverage and Capacity Solutions Group.

This column is an edited extract from CommScope's new eBook, 'LTE Best Practices'. Different authors of this eBook will contribute articles to this section.

Applying Modern Machine Vision Technologies to Security

By John Gabay, Mouser Electronics

Video surveillance has proven itself to be an advanced sensor with benefits. Serving as a remote set of eyes, video surveillance allows a virtual presence in off-site locations from a single point. What's more, video cameras cover a large contiguous swath of view, allowing a panning camera to steadily and consistently sweep a search pattern.

Video systems can also function in locations where humans cannot. The earliest known video surveillance technology was used to safely monitor the development and launch of V-2 rockets in 1942. From a safe distance, scientists and engineers could observe performances and identify failures.

Since then, video systems have acted as an extension of our eyes and ears. A steady stream of technology developments and manufacturing advancements have taken video surveillance to such a level that we feel comfortable relying on it for security purposes.

First Light

Light-sensitive materials can change their resistance or conductance based on the presence or absence of light. Early monochrome video systems like the RCA Vidicon camera system of the 1950s involved vacuum tubes featuring a light-sensitive selenium plate that acted as the focus of the image to be sensed.

An electron beam would scan the plate and the resulting current was directly proportional to the amount of light hitting that section of the plate at that exact time. Thus, the raster-scanned tube produced a rudimentary electronic video signal that could easily be transmitted long distances. The CRT television took this signal in reverse order, scanning a phosphor screen with the electron beam to re-create corresponding light levels in the image.

For decades, video was limited to monochrome sensing and displaying of images in real time. Color filters in front of each sensor limited the analog level to the intensity of the constituent colors in order to create color sensors. Color phosphors placed in the path of the electron beam were used to create colors. The advent of colorburst crystals helped to synchronize color components in the video signals.

Steady advances made improvements in these tubes over time, including better resolutions, lower power, lower cost manufacturing, and higher reliabilities. The Closed Circuit Television (CCTV) and broadcast industries were born and driving development at an even quicker pace.

On the down side, these technologies used fragile glass and the circuitry needed used higher voltages. Size constraints made tube-based image sensors a large and bulky assembly. Thanks to modern semiconductor technology, this is no longer the case.

Solid-State Sensors

Charge-Coupled Devices (CCDs) entered the scene in the early 1970s, combining semiconductor manufacturing with highly disciplined arrays refined through the use of memory devices. Individual light-sensitive picture-element sensors in the array synchronously set the state of a flip-flop. In turn, these sensors connected in a daisy-chain architecture coupled like a shift register. Clocking the shift register generates a synchronous video stream.

Initially used as one-dimensional sensor arrays for applications like scanners and fax machines, two-dimensional and eventually color versions of CCDs emerged, allowing video image sensors to dramatically shrink in size, while also simplifying power requirements.

Humans Need Not Observe

Because of the lack of availability of recording technologies, early CCTV systems needed human observers who had only one chance to extract as much information from a detected event as possible. After that, the images were lost forever.

In CCTV systems like this, it is the human who recognizes patterns, detects activities of interest, and makes the decision to create an alert or not. In essence, a human is the control processor in an alarm loop who makes the one-bit decision to trip an alarm machine or not.

Linear CCD sensors began to change this with the programmed ability to read bar codes and recognize patterns. Two-dimensional sensors used in modern phones, cameras, and machine-vision systems have extended resolutions and spectral

Horizontal Resolution	Vertical Resolution	Picture Elements	Single-Frame 24-bit	1 Second Buffer	Standard
320	240	76,800	230,400	6,912,000	1/4 VGA
640	480	307,200	921,600	27,648,000	VGA
800	600	480,000	1,440,000	43,200,000	SVGA
1024	768	786,432	2,359,296	70,778,880	XVGA
1280	768	983,040	2,949,120	88,473,600	WXGA
1280	1024	1,310,720	3,932,160	117,964,800	SXGA
1400	1050	1,470,000	4,410,000	132,300,000	SXGA+
2048	1536	3,145,728	9,437,184	283,115,520	QXGA
3200	1800	5,760,000	17,280,000	518,400,000	WQXTA+
4096	3072	12,582,912	37,748,736	1,132,462,080	HXGA
7680	4800	36,864,000	110,592,000	3,317,760,000	WHUXGA

Table 1:The increased resolutions impose dramatic memory requirements for video intensive processing, storage, and transmissions

sensitivities while reducing size, power, and the need for external lens assemblies.

Machine vision is joining with artificial intelligence to spawn a new generation of capable surveillance systems that require fewer personnel, less costs, and higher levels of programmed detections (and tracking) of targets. These requirements raise the bar for design engineers, who now need to integrate functions at a higher level with more processing power than ever before.

Design Issues and Concerns

Without the speeds and densities of modern memory devices, and without the horsepower of modern embedded processors, the next generation of smart surveillance systems could not be designed at reasonable costs and sizes. One main reason is the burden that every increase in image resolution imposes on the rest of the system design.

Older 8-bit 4-MHz legacy processors were fine for helping designers pioneer digital control loops, as well as digital techniques for signal processing and real time control, but are just not fast enough to tackle the needs of smart security. This basically boils down to the exponential growth of memory requirements.

For example, a simple legacy composite video camera had 525 total scan lines that could be sampled at various rates for each line. Twenty-one of those lines were used for vertical blanking. Modern CCD image sensors start at digital resolutions of ¼ VGA (320 x 240) at the low end.

At ¼ VGA resolutions, 76,800 bytes are needed to represent a single frame (at 8-bit resolution). With 8-bit RGB (one byte for red, green, and blue), this is up to 230,400 bytes. In both cases, this is beyond the addressable range of legacy processors.

Memory requirements rise dramatically as resolutions increase. Even at a VGA resolution of 640 x 480, a single monochrome frame needs 307,200 bytes, and color needs almost 1 Mbyte per single frame at 24-bit color palettes.

It doesn't stop here. At 30 frames per second, typical flicker fusion rates, almost 28 Mbytes are needed to buffer a single second of VGA video. A comparison of a few common video standard resolutions highlight this increasingly demanding constraint.

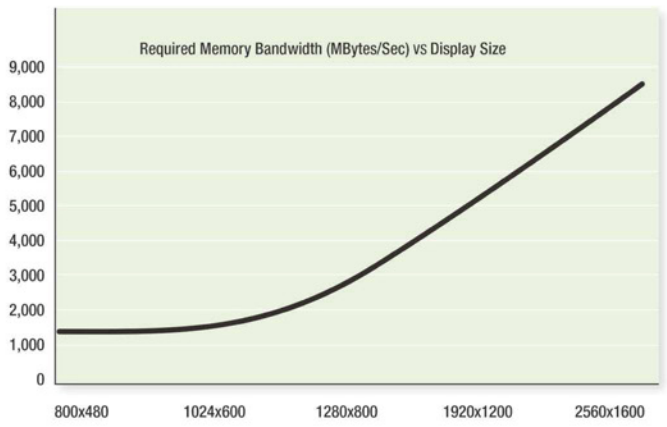

Figure 1: Transfer speeds and access times become increasingly more important as resolutions increase. This translates into faster processors and memory sub-systems to capture and buffer image data until it can be transported to a hub or aggregator

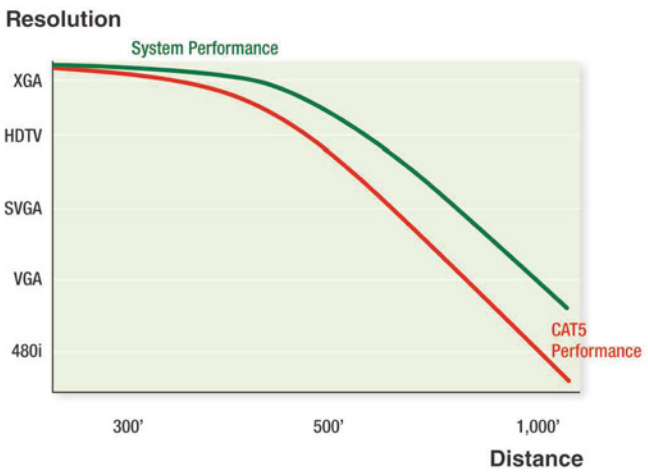

Figure 2: Even at lower video resolutions, data transfer speeds can degrade rapidly over distances using established low-cost media like CAT-style twisted pair cabling

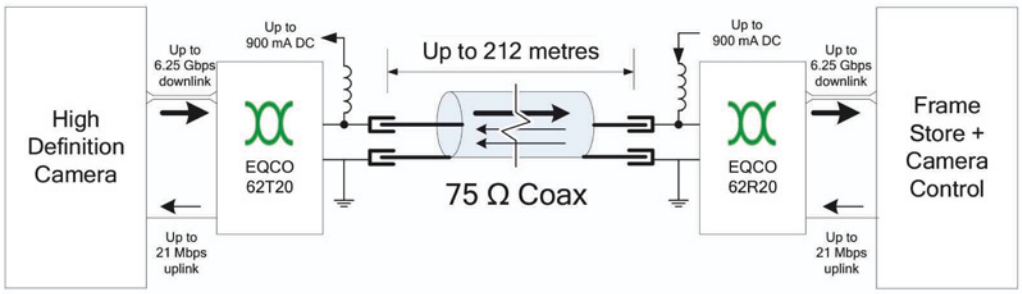

Figure 3: Microchip Technology's EQCO62X20 chipset is compatible with the CoaXPress v1.0 Camera standard

Blazing Processors

Several advanced processor families and architectures have evolved alongside video technologies and are now ready to step up to the plate and handle the next generations of smart surveillence and video designs. In all cases, external bus interfaces and most likely high-speed external DRAM will be used. Most advanced processors can handle several gigabytes of memory addressing and support several synchronous high-speed memory interfaces like DDR and SDR. Designers need to keep memory bandwidths in mind when architecting a system

Two main applications exist in which different requirements drive processor selection. The design of a central hub and/or aggregator necessitates very high-end or even multi-core processors, DVR functionality, and very deep pools of both volatile and non-volatile memory. However, a different set of constraints exist inside the actual cameras, including lower power, extended temperature ranges, and smaller sizes.

Running at 48 MHz with single-cycle instructions, the 32-bit ARM architecture in STMicroelectronics' STM32F051K4U6TR Cortex M0 processor has the data path and bus widths to handle entire picture element samples in a single transfer. It also runs down to 1.8 volts with a –40 to +85 degree operational range in a 5mm x 5mm package.

This processor has hardware direct memory access (DMA) that can handle five channels for memory-to-memory and memory-to-peripheral transfers and the built-in HDMI controller interface operates at lower speeds with minimal memory. A special clock domain for video is independent of the processor's main clock.

When the processor is coupled with modern high-speed and dense-memory devices like the ISSI DDR3 IS43TR16256AL-15HBLI, this device provides a single 4 Gbit (256 Meg x 16 bit) 1,333 MHz memory bandwidth solution. Keep in mind, it is not only a processor that needs to access and manipulate memory. The communications controller is an integrated part of this equation as well.

Transport and Linkage

Communications requirements can be a major part of next-generation surveillance system design challenges. With so much data, transfer speeds need to rise exponentially, as did memory requirements. The distance factor becomes an issue too. Even popular point-to-point 100 Mbit/sec Ethernet connections have limitations when driving long distances over CAT-style cabling.

This also means that shorter-distance data links like DVI and HDMI are not usable over these distances. The same holds true with many of the modern multimedia interconnections standards like S/PDIF and Toslink. While S/PDIF is digital and can be extended through the use of many standard driver and receiver chips, required data bandwidths are only going up, translating to a need for more elaborate and expensive driver technologies going forward.

Cameras with gigapixel resolutions are already available and in use. With the security and accountability concerns in modern society, people can begin to expect higher and higher resolutions to keep an eye on what they are doing. While fiber-optic links support higher bandwidths, copper has typically been cheaper to deploy. As a result, copper-based link technology is being developed and standardized for next-generation remote security systems.

One interesting technology that is rising to meet the bandwidth limitation challenge is the CoaXPress standard. CoaXPress is a coaxial cable-based standard for high-speed (6.25 Gbits/sec) point-to-point communications links well up to 130 meters. Multiple channels can up the data rate to 25 Gbits/sec.

Chipsets like the Microchip EQCO62X20 (EQCO62R20.3=Receiver, EQCO62T20.3 = Transmitter) can be used to form a bi-directional full-duplex communications channel over a single coaxial cable. Using external inductors, power can also be transferred over the same cable. Low power (<70 mWatt at 1.2 Volt) is desirable here too as is the small 4mm fine pitch-QFN packaging.

What About Wireless?

While wireless connectivity is possible, distance and bandwidth limitations make this unfeasible for most surveillance applications. In addition, wireless links are more easily jammed, making security applications vulnerable to attacks.

It may be possible to use short-hop wireless links to local aggregators and hubs. This is especially of interest if cloud-based connectivity is desired. It's not too far-fetched a notion that all civic cameras will become a part of the Internet of Things (IoT) in the very near future. This would mean that everyone would have access to all public surveillance devices to level the playing field and assure that no abuse of power or brutality will go unnoticed.

Conclusions

Security and surveillance are increasingly a part of our everyday lives. We are photographed, taped, and monitored in nearly everything we do. The sheer number of cameras and video feeds has driven the need for security personnel to sit and watch and make determinations.

Today's hardware systems cameras and video aggregators are and will continue to use higher-level processing and even AI to automate the data gathering and security assessments.

Smile, the camera focused on you is not so candid...

For further information: ***www.mouser.co.uk/applications***

Mouser Electronics, Authorised Distributor
Artisan Building, Suite C, First Floor, Hillbottom Road,
High Wycombe, Buckinghamshire, HP12 4HJ
Tel: +44 (0) 1494-467490
uk@mouser.com

Push the button

BY **MYK DORMER**

Low-power wireless has a very wide range of possible applications, but it is surprising just how many of them (once stripped of their obfuscations and complexities) come down to: "User pushes a button at location A, and something happens at location B".

That said, there is still an interesting collection of implications hiding in such a simple system, which can trip up both suppliers and customers alike. Response time of the system ranks very highly in that list.

When dealing with this simple specification (the time delay between the button being pushed and the "happening" actually occurring), I usually encounter one of two absolute polar opposites: either the requirement is quoted as "instant" or "it doesn't matter". In their way, both these specifications are equally wrong:

- **Too short.** It is (obviously) possible to specify and design radio control links that have very short latency. Simply using a high data-rate and a wideband wireless link capable of handling it will easily allow a short command burst to be transmitted in a couple of milliseconds or less.

  While this has some merit in reducing band usage, it involves a serious tradeoff in link range versus transmitter power, compared to slower systems built around narrowband radio hardware, while from an operational point of view it is pointless.

  Firstly, the activating time for any mechanical parts of a system will dominate any sub-ten-millisecond activation delay. Switch bounce in common push-button designs can exceed 10ms, and the activation time of the controlled device can also be significant (typical electromechanical relays take 5-20ms, while mechanical devices such as locks will take a significant fraction of a second).

  Then there are the contributions from user biology: Human reaction times (delay between seeing an event and acting on it) and cognitive delay (time taken to decide on an action and act) are both in the 200-300ms region. A typical user will be hard-pressed to notice a 100ms activation delay, even if the controlled device is a light – and even a half-second is barely noticeable.

> Human perceptions of time and delay don't necessarily match up with the practical requirements of a design, even if the observers are entirely aware of this fact

- **Too long.** At the other end of the spectrum, the issues are associated with user perceptions. A system which takes too long to activate (usually more of a problem in multiple-node, multiple-hop network architectures) will be perceived as defective or inadequate by the user, even if this is not the case.

  A good example would be an evacuation alarm for a large building. A 30s delay between activating one of the input devices and the alarm sounders going off throughout the site is irrelevant, compared to the time required to move hundreds of people down corridors and stairs, and out of the immediate area, but if demonstrating such a system to a potential user on a conference table the same 30s would seem ludicrously long.

  The situation in this case is that human perceptions of time and delay don't necessarily match up with the practical requirements of a design, even if the observers are entirely aware of this fact. Subjectively, any delay exceeding four or five seconds will feel excessive, while shorter periods will usually go unremarked on.

The upshot of these observations is quite simple: when specifying a control system that places a human in the loop, be aware of both the limitations and irrational perceptions of that component but, within those limits, design for the best performance your hardware budget allows and don't pay for short response times you don't need. Faster is not always better. ●

Myk Dormer, Consultant Engineer, Radiometrix Ltd
www.radiometrix.com

DESIGN AND COMPARISON OF MIMO OFDM FOR DIFFERENT TRANSMISSION SCHEMES

ARUN KUMAR AND **MANISHA GUPTA** FROM JECRC UNIVERSITY IN JAIPUR, INDIA, ANALYZE A MIMO-OFDM SYSTEM FOR DIFFERENT MODULATION SCHEMES

Orthogonal frequency division multiplexing (OFDM) is a method of encoding digital data on multiple carrier frequencies – a popular scheme used in modern-day communications. Combined with the multiple input, multiple output (MIMO) method, MIMO-OFDM plays an important role in increasing capacity and data rates by minimizing co-channel and multipath interference.

An MIMO-OFDM receiver typically includes a large number of array antennas which receive the same signal via different paths. Capacity can also be increased by sending different data at the same time.

Using adaptive modulation and schemes with high data rates, sub-carrier allocation can further increase the efficiency of a MIMO-OFDM system. However, one major disadvantage of MIMO OFDM is that it consumes a lot of power, also increasing the overall costs.

Here, we present a design of a 4 x 8 MIMO-OFDM system with equalization and orthogonal space-time block code (OSTBC) for different transmission schemes. We have limited the system to 4 x 8 antennas since MAT-LAB/SIMULINK allow a maximum number of four antennas at the transmitter and eight at the receiver.

We will describe the design and implementation of a MIMO-OFDM system for several different modulation schemes – BPSK (Binary Phase-Shift Keying), QPSK (Quadrature Phase Shift keying) and M-QAM (Quadrature Amplitude Modulation for M = 16, 64 and 256); see Figures 1-5.

We will consider an array of antennas that receives the highest frequency signal at the input. For sampling, higher frequency signals are converted into an intermediate frequency (still as analog signals), which will be converted into a digital signal by a high-speed analog-to-digital converter (ADC). Then, the sampled signals are passed for direction of arrival (DOA) estimation. Following that, a beam-forming weight is calculated and applied to the array of antennas. Finally, all received signals are summed and demodulated.

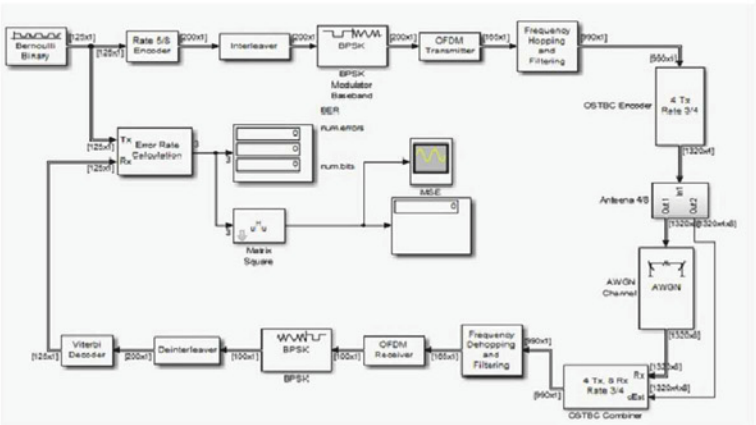

Figure 1: Proposed OFDM-simulation for the BPSK modulation scheme

System Setup

Implementation of a MIMO-OFDM system involves a large number of components, such as antennas, equalizers and a complex encoder-decoder system, all of which add to its complexity and cost.

MMSE Equalizer

Minimum means square error (MMSE) is a linear equalizer, typically used when the channel and noise information are accurately known by the receiver. It does not completely reduce inter-symbol interference (ISI), but it reduces the parameters that cause ISI, and also minimizes the noise power and mean square error of the signals.

Orthogonal Space Time Block Code (OSTBC)

Space time block code (STBC) is used for both spatial and temporal diversity codes., to reduce the effect of fading and noise that degrade signal quality. It encodes data into a block earlier in the transmission, which is then sent via several antennas.

In our work the transmitted signal is encoded at a rate of 3/4 using the following matrix:

$$\begin{pmatrix} s_1 & s_2 & s_3 & 0 \\ -s_2^* & s_1^* & 0 & s_3 \\ s_3^* & 0 & -s_1^* & s_2 \\ 0 & s_3^* & -s_2^* & -s_1 \end{pmatrix}$$

MIMO Antenna

A smart antenna is used for the uplink, whereas for the downlink multiple antennas are used. Currently, the 900, 1800 and 1900MHz bands are allocated for smart antenna use.

The MIMO antenna plays an important role in increasing the efficiency of a MIMO-OFDM system, and interference can be further reduced by using a beam-forming concept, where the beam of an antenna follows the user in a desired direction. The main beam of the antenna tracks the user continuously and, at the same time, the interference is directed towards the null, which reduces its effect.

Transmitted Signal

The spectra of BPSK, QPSK, 16-QAM, 64-QAM-64 and 256-QAM transmitted signals are shown in Figures 6-10, created by a Bernoulli binary generator.

For BPSK, shown in Figure 6, the maximum peaks are 4.907V at 0.076GHz, 3.608V at 0.225GHz and 3.582V at 0.208GHz. The channel power is 21.141dBm, with occupied bandwidth of 508.3087MHz and frequency error of -58.8279kHz.

For QPSK (Figure 7), the maximum peaks are 3.291V at -0.122GHz, 3.092V at -0.39GHz and 2.550V at 0.233GHz. The channel power is 21.141dBm, with occupied bandwidth of 508.3904MHz and frequency error of 58.8279kHz.

For 16-QAM (Figure 8), the maximum peaks are 8.247V at 0.233GHz, 8.16V at -0.233GHz and 7.489V at 0.255GHz. The channel power is 23.380dBm, with occupied bandwidth of 547.3575MHz and frequency error of -1.2503MHz.

For 64-QAM (Figure 9), the maximum peaks are 9.595V at 0.233GHz, 9.095V at -0.225GHz and 10.264V at -0.233GHz. The channel power is 23.810dBm, with occupied bandwidth of 555.0144MHz and frequency error of 724.7183kHz.

For 256-QAM (Figure 10), the maximum peaks are 9.595V at 0.233GHz, 9.095V at -0.225GHz and 10.264V at -0.233GHz. The channel power is 23.810dBm, with occupied bandwidth of 555.0144MHz and frequency error of 724.7183kHz.

Received Signal

The spectra of the BPSK, QPSK, 16-QAM, 64-QAM and 256-QAM received signals are shown in Figures 11-15, obtained by demodulating the modulated wave.

The figures show maximum peaks when there is excellent coverage, medium peaks for good coverage and zero peak corresponding to poor coverage.

For BPSK (Figure 11), the maximum peaks are -92.034V at 0.182GHz, -93.012V at 0.208GHz and -93.089V at 0.233GHz. The channel power is -8.091dBw, with occupied bandwidth of 526.9263MHz and frequency error of 9.9328MHz.

For QPSK (Figure 12), the maximum peaks are -93.742V at 0.141GHz, -93.343V at 0.243GHz and -92.570V at 0.233GHz. The channel power is -9.066dBm, the occupied bandwidth is 531.2848MHz and frequency error 9.6727MHz.

For 16-QAM (Figure 13), the maximum peaks are -85.972V at

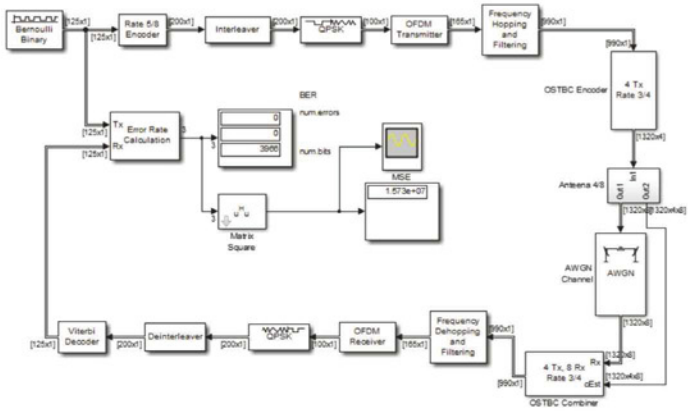

Figure 2: Proposed OFDM-simulation for the QPSK modulation scheme

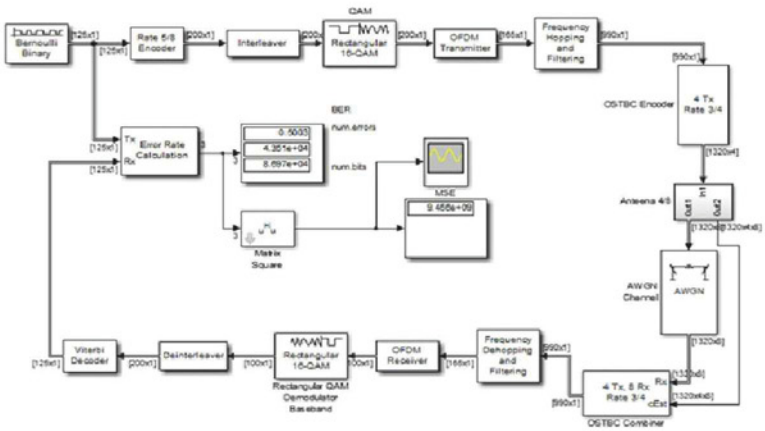

Figure 3: Proposed OFDM-simulation for the 16-QAM modulation scheme

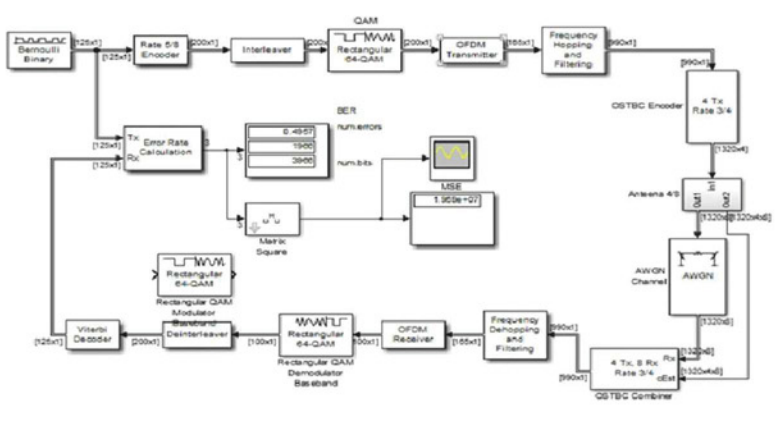

Figure 4: Proposed OFDM-simulation for the 64-QAM modulation scheme

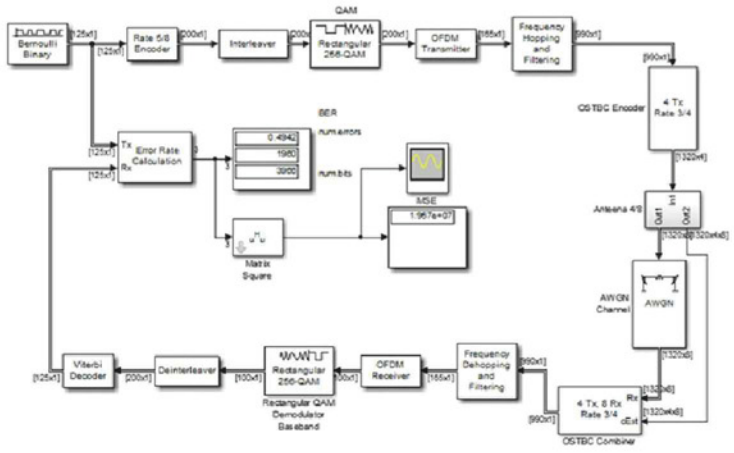

Figure 5: Proposed OFDM-simulation for the 256-QAM modulation scheme

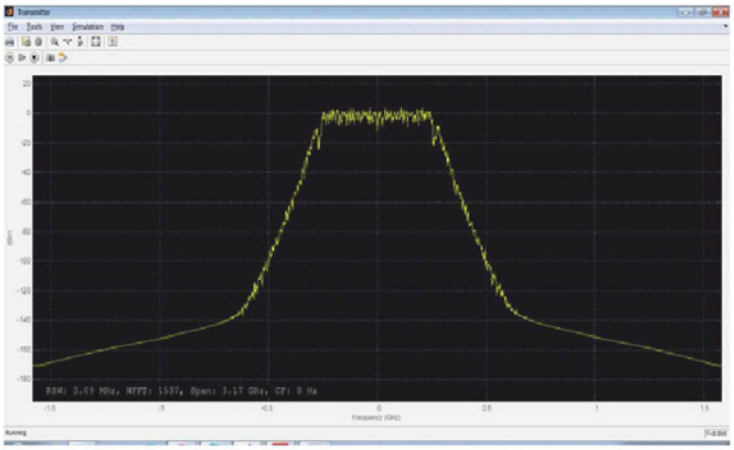

Figure 6: Transmitted signal for the BPSK modulation scheme

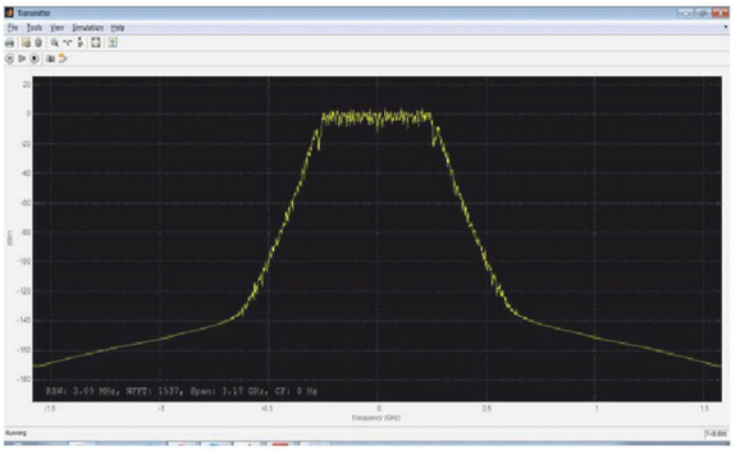

Figure 7: Transmitted signal for the QPSK modulation scheme

-0.224GHz, -86.060V at -0.233GHz and -57.739V at -1.291GHz. The channel power is -6.552dBw, the occupied bandwidth is 552.814MHz and frequency error -8.0484MHz.

For 64-QAM (Figure 14), the maximum peaks are -85.129V at -0.224GHz, -84.896V at -0.233GHz and -88.437V at -1.291GHz. The channel power is -6.2dBm, occupied bandwidth is 554.8577MHz and frequency error 8.2803MHz.

For 256-QAM (Figure 15), the maximum peaks are -85.129V at 0.224GHz, -84.896V at -0.233GHz and -88.437V at -1.291GHz. The channel power is -6.328dBm, the occupied bandwidth is 554.8577MHz and frequency error 8.2415MHz.

MMSE Plot

We plot the MMSE-equalizer output as amplitude vs time; the error is reduced and ISI minimized.

The MMSE value of BPSK is $2.74e^{+10}$; the maximum peak is 27.399V at T = 1ms, with peak-to-peak given by 27.399 meters and root mean square (RMS) value of 11.792m. As shown in Figure 16, the amplitude increases exponentially with time.

The MMSE value of QPSK is $2.18e^{+10}$; the maximum peak is 15.729V at T = 100µs, with peak-to-peak 15.299 meters and the RMS value 3.26m. As shown in Figure 17, the amplitude increases exponentially during the rise time of 11.02µs.

The MMSE value of 16-QAM is $2.737e^{+10}$; maximum peak is 27.373V at T = 1ms, with peak-to-peak 27.373m and the RMS value is 11.782m. As shown in Figure 18, the amplitude insreases exponentially during the rise time of 408.805µs.

The MMSE value of 64-QAM is $2.735e^{+10}$; maximum peak is 27.351V at T = 1ms, with peak-to-peak 27.351m and RMS value of 11.774m. As shown in Figure 19, the amplitude increases exponentially during the rise time of 402.636µs.

The MMSE value of 256-QAM is $2.736e^{+10}$; the maximum peak is 27.351V at T = 1ms, with peak-to-peak 27.351m and the RMS value is 11.774m. As shown in Figure 19, the amplitude increases exponentially during the rise time of 402.636µs.

Input And Output Constellations

The constellation diagrams for the BPSK, QPSK, QAM-16, QAM-64 and QAM-256 schemes are shown in the Figures 21-25 and their respective output constellation plots in Figures 26-30.

BER PLOT

The simulation shows that the bit error rate (BER) of QPSK is zero, which means this is the best and most robust modulation technique compared to the other schemes discussed here. BER is zero due to the efficient design of the 4 x 8 antenna system, and because we used a good encoder and decoder.

The simulation also shows that BER of 16-QAM, 64-QAM and 256-QAM are approximately the same, i.e. around 0.4992, which proves that the proposed design is more robust for use in modulation techniques.

The BER is shown in Figure 31. ●

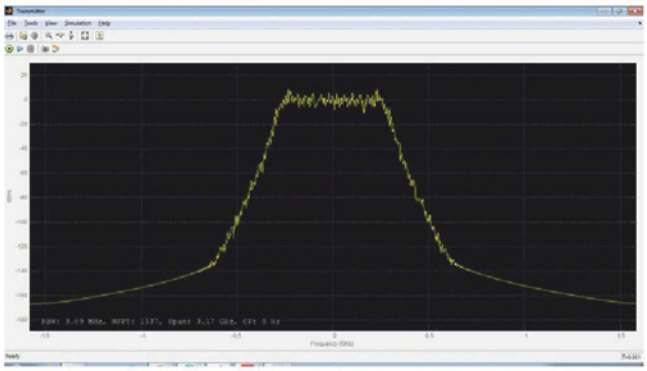

Figure 8: Transmitted signal for the 16-QAM modulation scheme

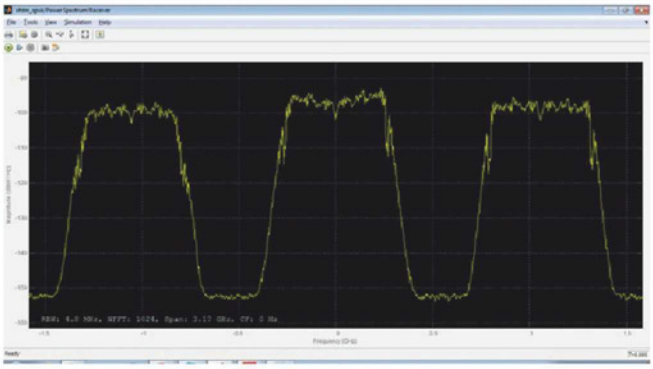

Figure 12: Received signal for the QPSK modulation scheme

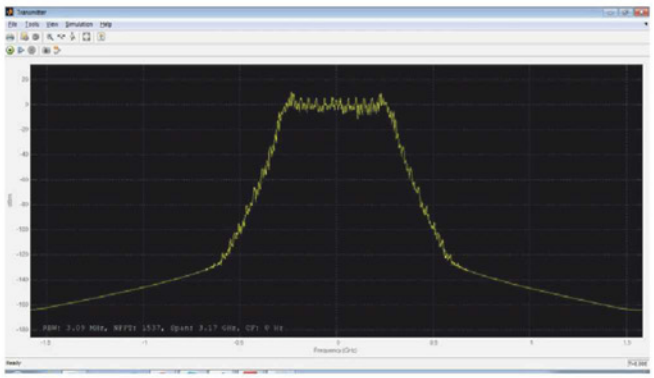

Figure 9: Transmitted signal for the 64-QAM modulation scheme

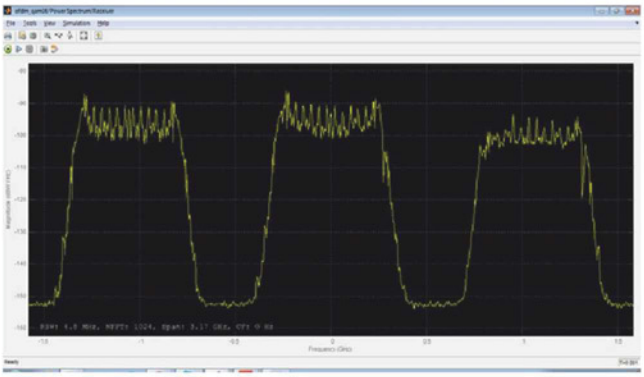

Figure 13: Received signal for the 16-QAM modulation scheme

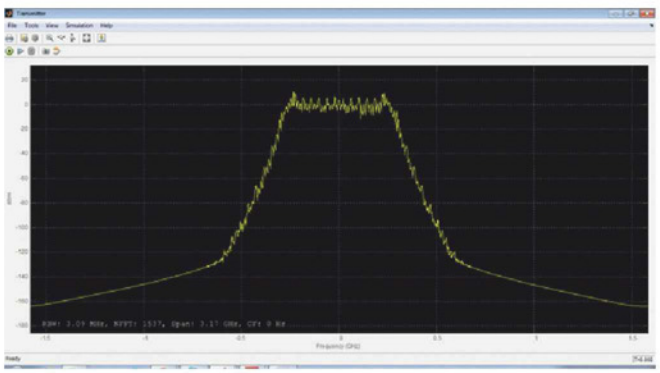

Figure 10: Transmitted signal for the 256-QAM modulation scheme

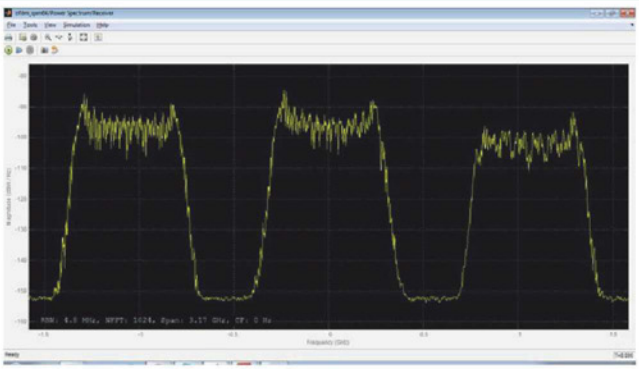

Figure 14: Received signal for the 64-QAM modulation scheme

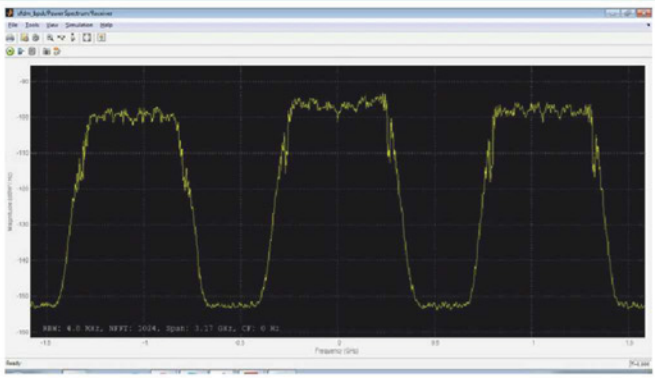

Figure 11: Received signal for the BPSK modulation scheme

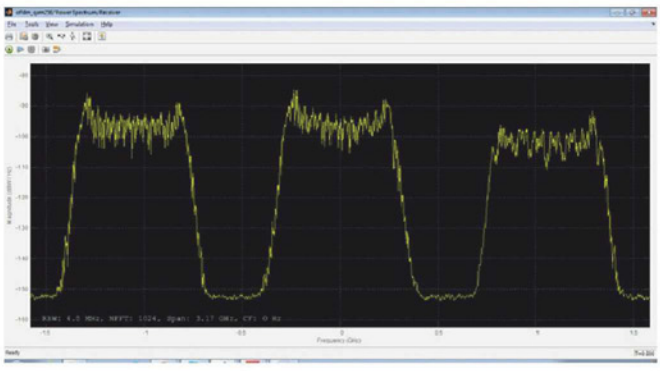

Figure 15: Received signal for the 256-QAM modulation scheme

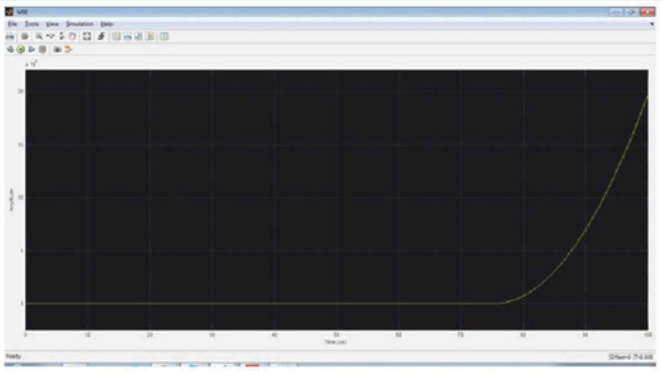

Figure 16: An MSE plot for the BPSK modulation scheme

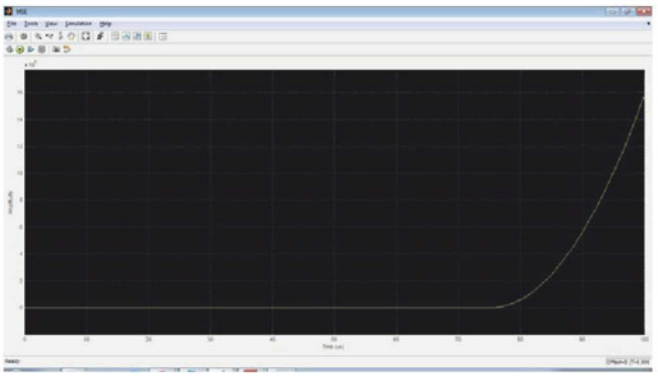

Figure 17: MSE plot for the QPSK modulation scheme

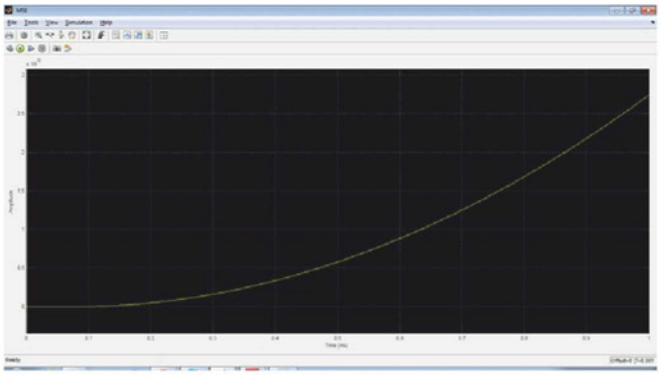

Figure 18: MSE plot for the 16-QAM modulation scheme

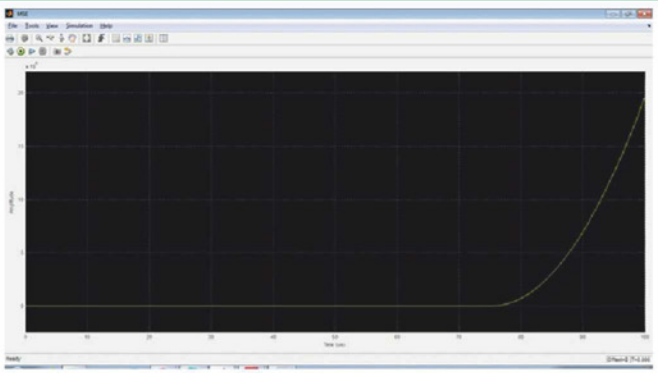

Figure 19: MSE plot for the 64-QAM modulation scheme

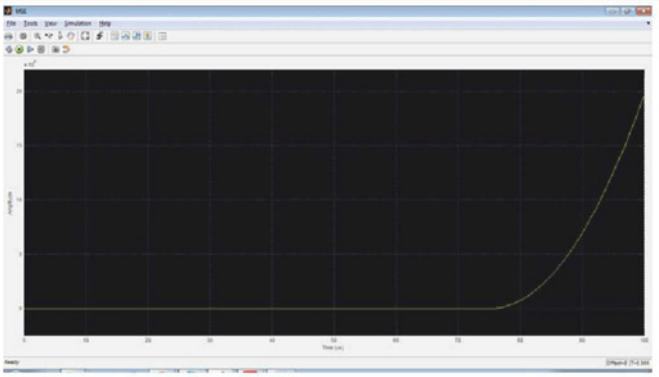

Figure 20: MSE plot for the 256-QAM modulation scheme

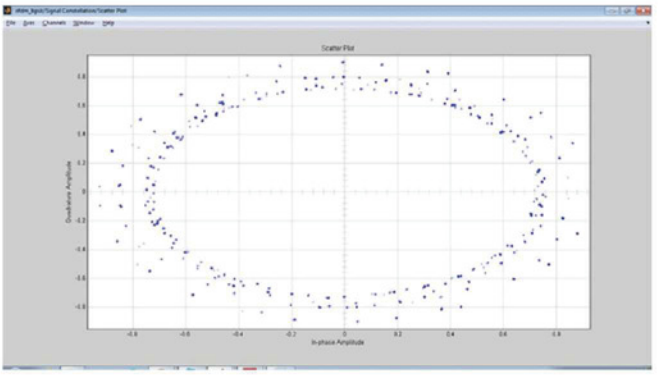

Figure 21: Input constellation diagram of BPSK modulation scheme

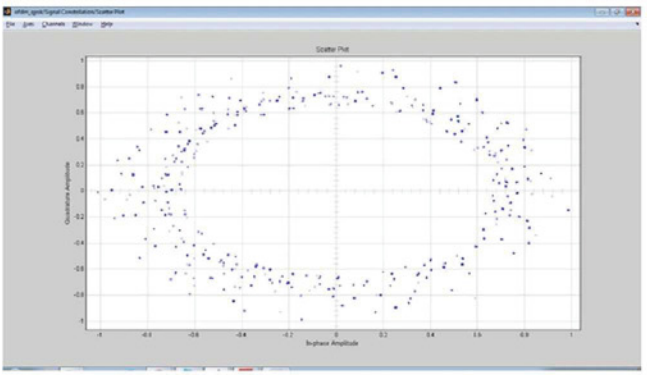

Figure 22: Input constellation diagram of QPSK modulation scheme

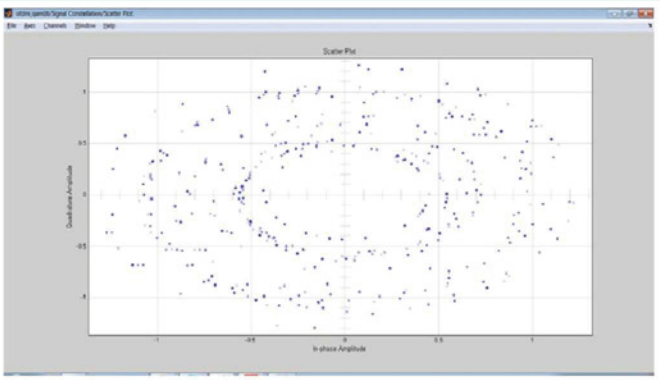

Figure 23: Input constellation diagram of 16-QAM modulation scheme

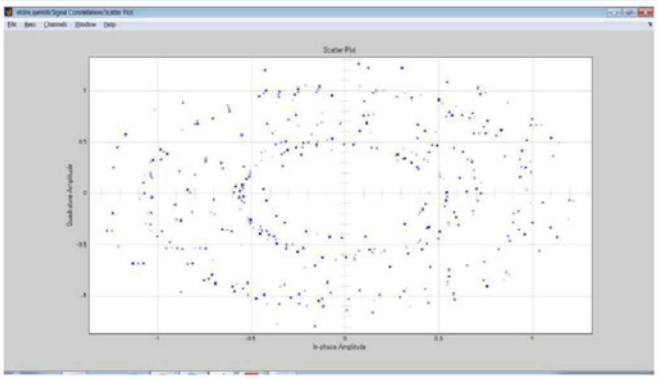

Figure 24: Input constellation diagram of 64-QAM modulation scheme

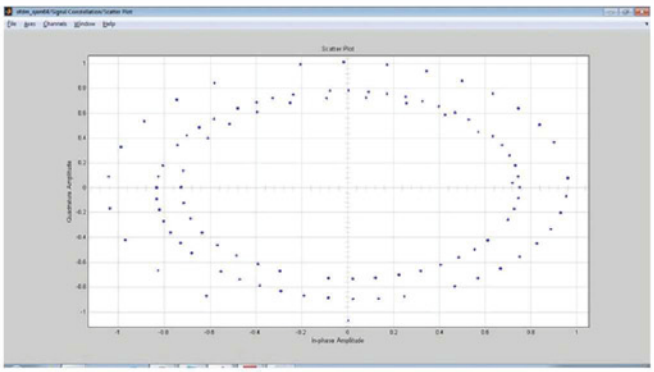

Figure 25: Input constellation diagram of 256-QAM modulation

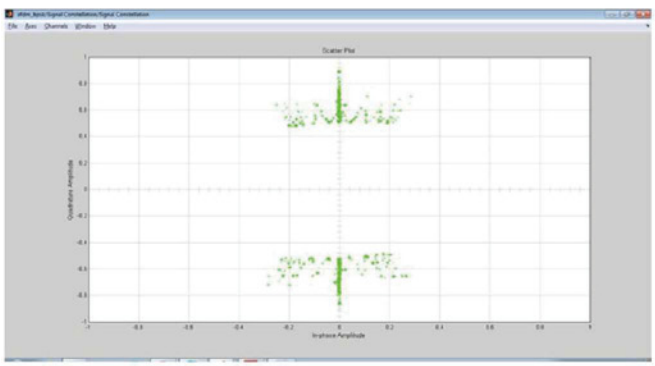

Figure 26: Received constellation diagram for BPSK modulation

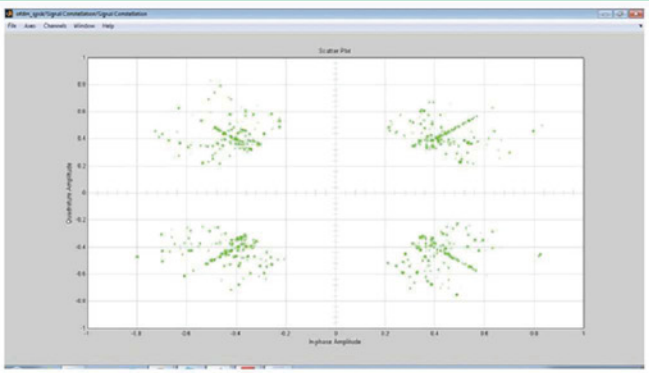

Figure 27: Received constellation diagram for QPSK modulation

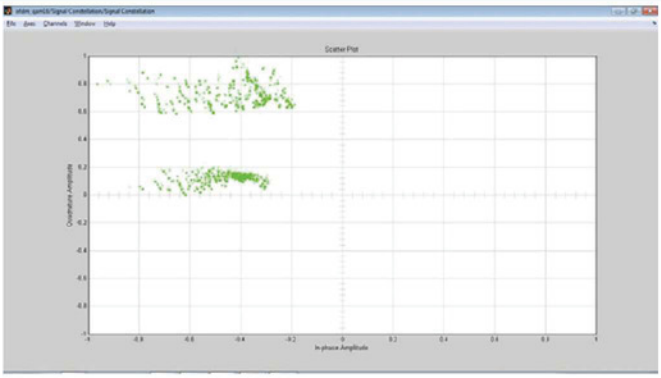

Figure 28: Received constellation diagram for 16-QAM modulation

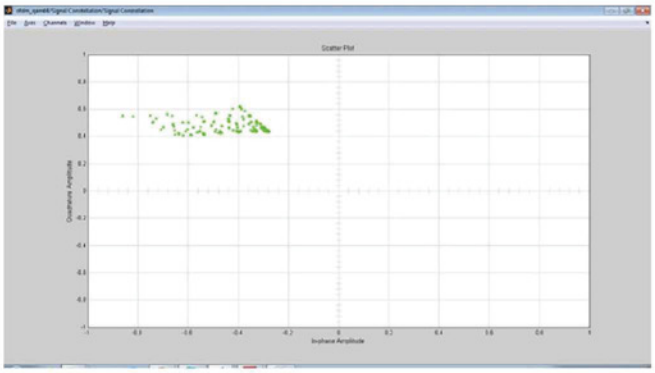

Figure 29: Received constellation diagram for 64-QAM modulation

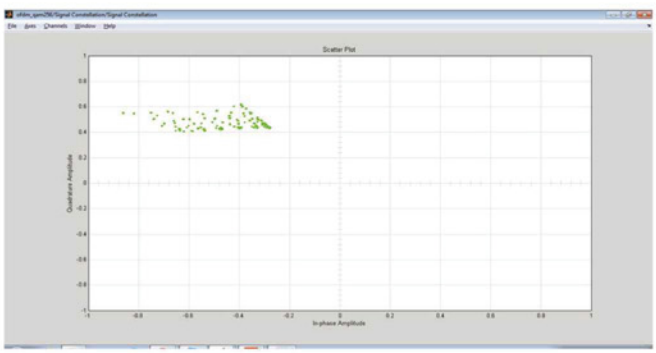

Figure 30: Received constellation diagram for 256-QAM modulation

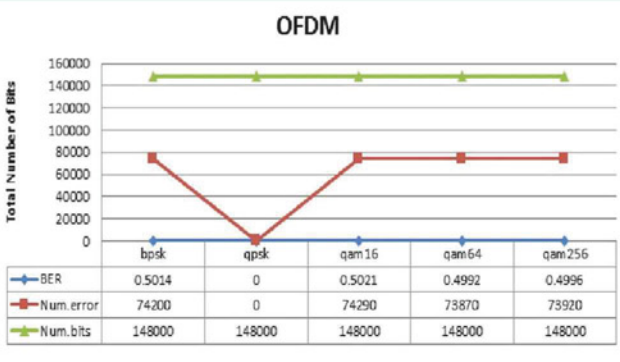

	bpsk	qpsk	qam16	qam64	qam256
BER	0.5014	0	0.5021	0.4992	0.4996
Num.error	74200	0	74290	73870	73920
Num.bits	148000	148000	148000	148000	148000

Figure 31: BER plot

5G MOBILE-HANDSET MIMO ANTENNA BASED ON SMALL PHASED ARRAYS

PAN SONG, YANAN XIE, DENGKE PAN AND **ZHIKUN LIU** FROM SHANGHAI UNIVERSITY DESCRIBE THEIR MIMO ANTENNA, BASED ON TWO VERTICALLY-PLACED SMALL PHASED ARRAYS AT 28GHZ, SUITABLE FOR 5G MOBILE HANDSETS

5G is the abbreviation for 5th generation mobile communications, although it is not quite an official term used in technical specifications yet. Most of the spectrum for cellular mobile systems is concentrated in the bands below 6GHz, which is now beginning to cause a severe spectrum crisis. Yet, high cell capacity and data rates of several gigabits per second are required for the next generation of mobile communications to accommodate the rapidly increasing user demands. This has motivated the exploration of communications in the millimeter-wave frequency range, which offers a wider bandwidth and uses smaller antennas.

Many companies and academics are actively engaged in this exploration, and South Korea's Samsung Electronics has already achieved a peak download speed of 1Gbps at 28GHz, by employing adaptive beam-forming technology with 64 working antennas, making it a suitable technology candidate for urban environments.

The 28GHz band has a clear advantage over 60GHz and above because it exhibits better propagation characteristics and free space path loss.

Smart antenna technologies (such as adaptive beam-forming and MIMO) and millimeter-wave communications are expected to play key roles in 5G systems.

Antenna Design

MIMO antennas based on phased arrays can realize beam scanning in space with higher gains, improving efficiencies; as such this is a feasible approach for use in future mobile handsets.

Shown in Figure 1 is our MIMO antenna design, which consists of two vertically placed linear phased arrays with eight and six elements respectively.

A linear phased-array antenna is the simplest and most commonly used structure in its class. Theoretical analyses have shown that a phased-array antenna can produce a beam in any direction by assigning different amplitudes and phases to each element in the array.

For convenience, in our proposed antenna design the 8-element array will be Array 1 and the 6-element array will be Array 2. In Array 1, units 1-8 are counted from left to right (see Figure 1), and in Array 2, units 1-6 are counted from the bottom up.

A unit in an array is a planar inverted-F antenna (PIFA), one of the main forms of the traditional mobile phone antenna due to its low profile, ease of manufacture and low cost (see Figure 2).

A planar inverted-F antenna consists of a patch parallel to the ground and two vertical strips, one used for the feed and the other for grounding. The antenna is matched by adjusting the distance between the two strips; whereas adjusting the size of the patch fixes the unit's operating frequency around 28GHz and achieves impedance bandwidth of 2.6GHz (between 26.7GHz to 29.3GHz) with return loss of less than 7.5dB. The unit's return loss is shown in Figure 3.

For our design we chose a 55mm x 110mm ground plane. The antenna is positioned on a 0.5mm thick Rogers RT substrate with a relative permittivity of 2.2 and loss tangent of 0.02.

To reduce the total volume, the substrate is embedded between

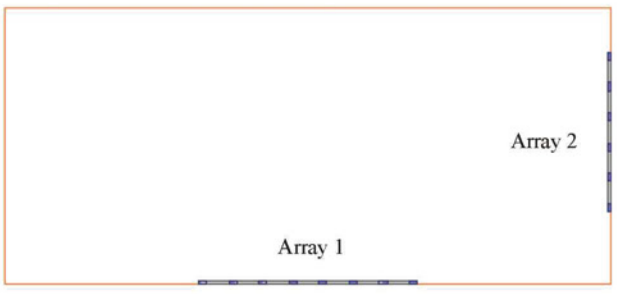

Figure 1: The geometry of the proposed antenna

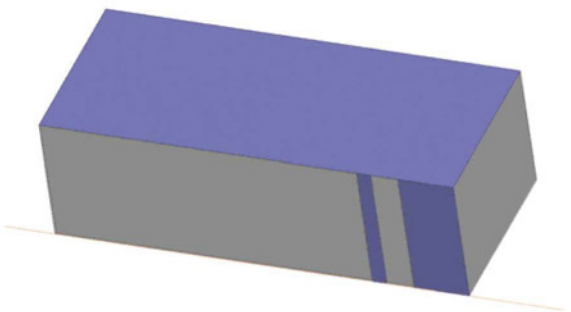

Figure 2: The configuration of the PIFA antenna

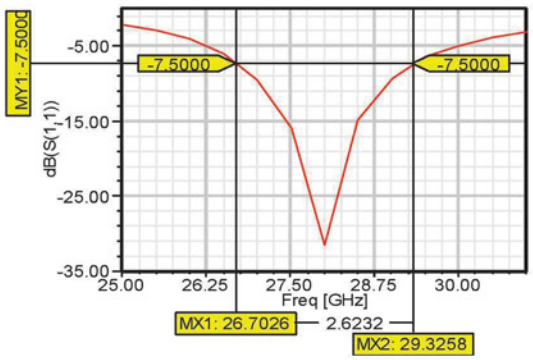

Figure 3: The unit's return loss

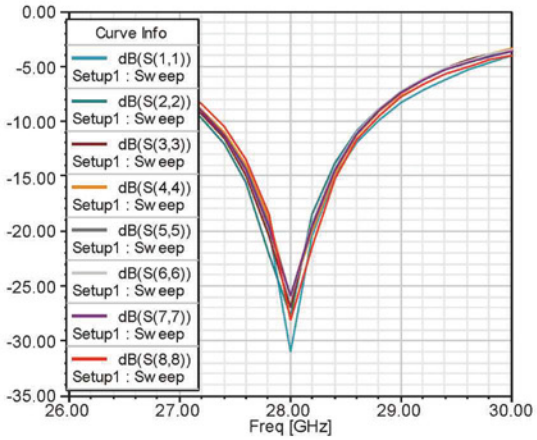

Figure 4: Return losses of Array 1

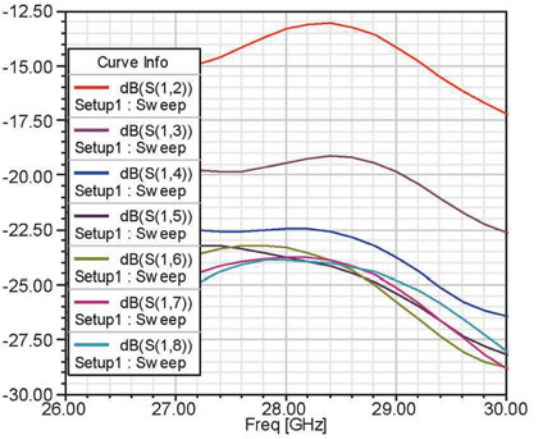

Figure 5: S parameters of Unit 1 in Array 1

the antenna and the ground plate, covering an area only as large as the antenna itself. The covered substrate area under Array 1 is around 40 x 0.65mm² and 30 x 0.65mm² under Array 2.

Operating frequency of the array's first and last units will change a little because of the influence of ground. The operating frequency can be adjusted as required by changing the dimensions of the substrate under the first and last units.

It should be also noted that unit 8 in Array 1 is also influenced by Array 2 and, reciprocally, unit 1 by Array 2. On the other hand, Array 1 is placed parallel to ground, so the ground's impact is greater on Array 1 than Array 2. Through optimization, we add 0.52mm substrate on the left side of unit 1 in Array 1, and 0.4mm on the bottom of unit 1 in Array 2. The distance between the units is set to 0.51λ in the two arrays.

As the position of a mobile handset is constantly changing, the distance and direction between its antennas and base stations also changes. The two arrays can work together or alternately to ensure the mobile phone antenna's main beam scans in three dimensions, fully covering the horizontal and vertical planes and certain angles around them. So, regardless of the mobile phone's location, the antenna's main lobe will always point in a specific direction.

For an array antenna, there is a certain tradeoff to be considered between side-lobe levels and the width of the main lobe. The optimal radiation pattern is defined as follows: for a given width of the main lobe, the side lobe level can be as low as possible; for a given value of the side lobe level, the width of the main lobe can be as wide as possible. Theoretical analysis suggests that when the distribution of the excitation source complies with the Dolph-Chebyshev function (which refers to a maximum main-lobe width for a given side-lobe attenuation), the radiation pattern of the antenna will be close to the optimal radiation pattern. Based on proven theory, in this study we applied the Dolph-Chebyshev distribution to the signal source of the arrays.

> Theoretical analyses have shown that a phased-array antenna can produce a beam in any direction by assigning different amplitudes and phases to each element in the array

Experimental Results

The simulated results were obtained with the Ansoft HFSS software. Figure 4 shows the simulated S parameters of Array 1, which are in good correspondence with return loss of less than 25dB around 28GHz. The return loss of less than 7.5dB covers 2GHz in the 27-29GHz range.

We also checked the other S parameters of Unit 1 in Array 1, as shown in Figure 5. It can be seen that, in addition to S12 whose peak value reaches -13dB, the other coupling coefficients of Unit 1 are all below 19dB. Low coupling coefficients indicate a low inter-unit effect, which means they work well individually.

The radiation gain and beam scanning of Array 1 are shown in Figures 6 and 7 respectively. It can be seen that Array 1's main beam can scan from -40° to +40° off the broadside direction with gain of 10.4dBi at 28GHz.

Array 2's experimental results of are shown in Figures 8-11. The return losses and coupling coefficients also show good matching, with wide frequency bandwidth and low insertion loss. The return loss of less than 7.5dB also covers 2GHz from

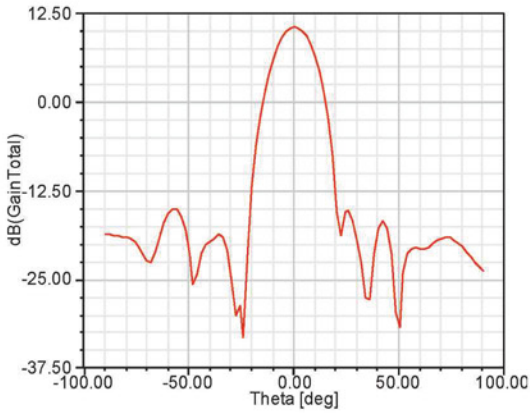

Figure 6: Total radiation gain of Array 1

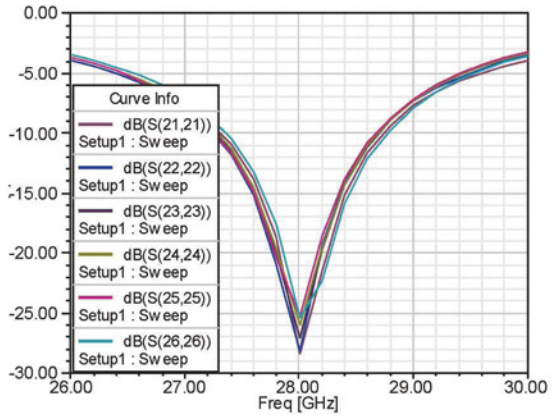

Figure 8: Return losses of Array 2

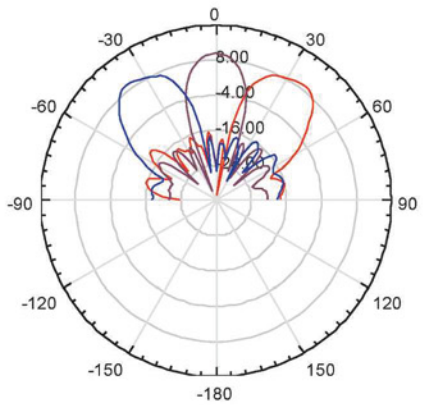

Figure 7: Beam scanning of Array 1

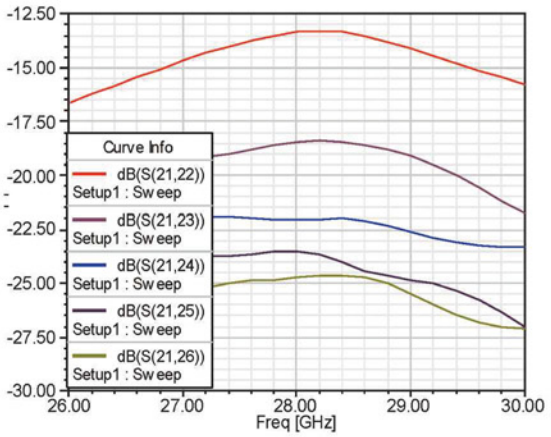

Figure 9: S parameters of the Unit 1 in Array 2

27-29GHz. The curves of other S parameters of unit 1 in Array 2 indicate that, in addition to S12 whose peak value reaches -13dB, the other coupling coefficients of unit 1 are all below -18dB.

Array 2's main beam can scan from -35° to +35° off the broadside direction with a gain of 7.5dBi at 28GHz.

The antenna's operating principle is shown in Figures 12 and 13. Figure 12 shows the handset placed vertical to the ground plane. When Array 1 radiates in a broadside direction, its radiation pattern covers the whole horizontal plane, as shown in Figure 12a; and when Array 2 radiates in a broadside direction, its radiation pattern covers the whole vertical plane, as shown in Figure 12b. By assigning different phases to the feeding point, both arrays can scan their main lobe in space, as shown in Figures 12c and 12d. The operating principle is similar to when the handset is placed parallel to the ground plane as shown in Figure 13.

So, our study shows that the two arrays work together or alternately to ensure the main lobe of the mobile device's antenna always points in a specific direction when the position of the device arbitrarily changes. In addition, the occupied

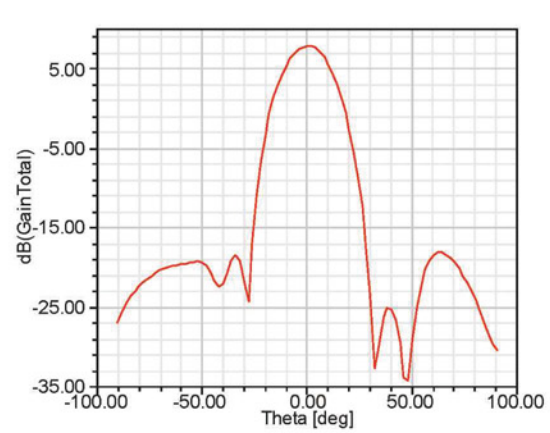

Figure 10: Total radiation gain of Array 2

volume of the proposed antenna is small, yet the performance is good. Good simulation results indicate its feasibility for future 5G terminal antennas.

The only caveat is that we studied this antenna in theory, without verifying it physically. ●

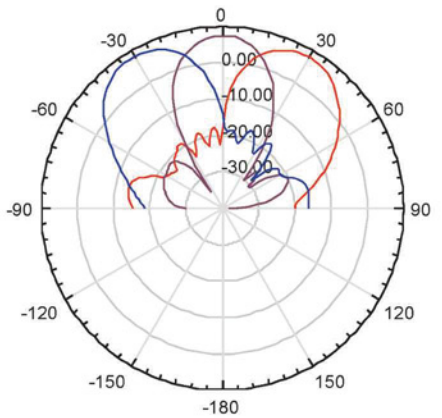

Figure 11: Array 2's beam scanning

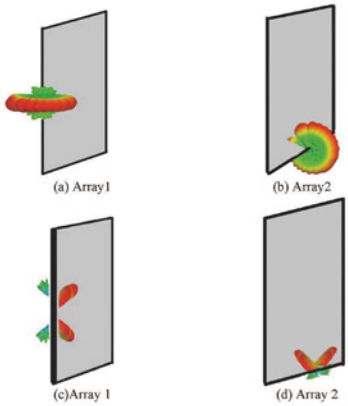

Figure 12: Antenna radiation pattern illustration 1

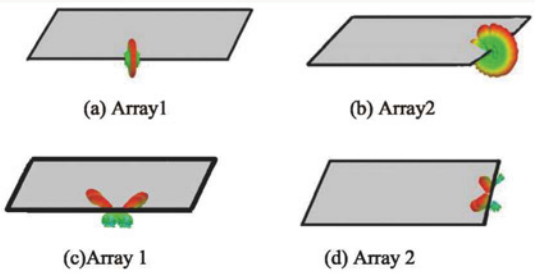

Figure 13: Antenna radiation pattern illustration 2

CHARACTERISTICS OF MICROWAVE AND RF SIGNAL FILTERS

BY **STOJCE DIMOV ILCEV** FROM DURBAN UNIVERSITY OF TECHNOLOGY IN SOUTH AFRICA

Microwave (MW) and RF bandpass filters allow through frequencies within a certain range and reject or attenuate frequencies outside that range. Examples of analogue electronic bandpass filters are an RLC circuit (resistor/inductor/capacitor) or an RC circuit. Bandpass filters can also be created by combining lowpass filters with highpass filters.

'Bandpass' is different from 'passband' as it refers to an actual portion of affected spectrum, hence one might say "a dual bandpass filter has two passbands". An ideal bandpass filter has a completely flat passband (e.g. no gain or attenuation throughout), and would completely attenuate all frequencies outside the passband.

However, in practice no bandpass filter is ideal and it does not attenuate completely all the frequencies outside the desired frequency range. In particular, there is a region just outside the intended passband where frequencies are attenuated but not rejected. This is known as the filter roll-off, usually expressed in dB of attenuation per octave or decade of frequency.

Generally, the design of a filter seeks to make the roll-off as steep as possible, thus allowing the filter to perform as close as possible to its intended design. Often, this is achieved at the expense of passband or stopband ripple.

Filters Categorization

In general, all filters have the property of removing unwanted frequencies from a signal. They can be divided into two classes: passive (made of capacitors, resistors, inductors) and active (involving an amplifier). Filters can be further categorized into four types: lowpass (removes high frequencies), highpass (removes low frequencies or DC), bandpass (removes a range of frequencies on both sides of a band) and notch, reject or bandstop (removing frequencies in the middle), see Figure 1.

The bandwidth of a filter is simply the difference between the upper and lower cutoff frequencies. The shape factor is the ratio of bandwidths measured using two different attenuation values to determine the cutoff frequency; e.g. a shape factor of 2:1 at 30/3dB means the bandwidth measured between frequencies at 30dB attenuation is twice that measured between frequencies at 3dB attenuation.

Terminology parameters of a MW/RF filter design are signal-to-noise (S/N) ratio; the bandwidth is a range of frequencies as G(jw) > 0.707; the cutoff frequency is of passband frequency; and the break point of a filter is the point of -3dB.

The signal-to-noise (or signal-to-interference) ratio, S/N (or SNR) is defined as:

$$\mathbf{S/N = 20log_{10}\,(E_{th}/V_{SM}) = 10log_{10}\,(W_S/W_N);\ in\ dB}$$

where W_S and W_N are the signal and noise power respectively, while E_{th} and V_{SM} are the root mean square (rms) values of the voltages. Thus, G(jw) is a complex number for any angular frequency, w, so its plot consists of complex numbers.

Bandpass Filters

One simple use for passive filters is in audio amplifiers, loudspeaker crossover filters and pre-amplifier tone controls among others, see Figure 3A.

Active bandpass filters are slightly different in that they are

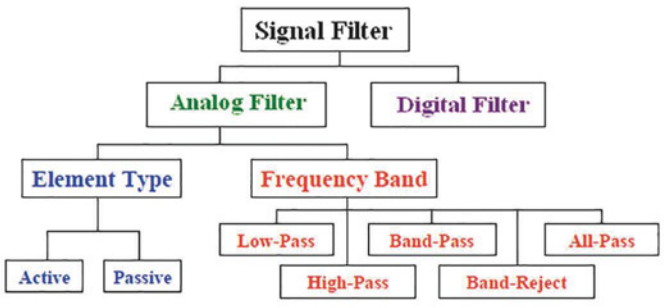

Figure 1: Classification of MW and RF filters

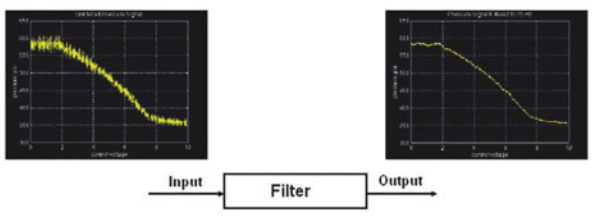

Figure 2: Outline of a filter design

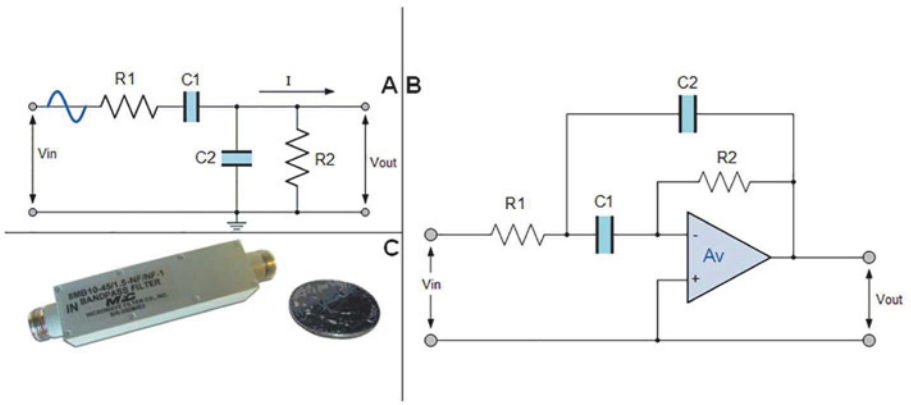

Figure 3: Passive and active bandpass filter circuit and amplitude

frequency-selective filter circuits used in electronic systems to separate a signal at a particular frequency or a range of signals that lie within a certain band of frequencies; see Figure 3B. An active filter uses active components, such as amplifiers, to improve the performance and predictability of a filter, whilst avoiding the use of inductors, which are typically expensive compared to other components.

> In general, all filters have the property of removing unwanted frequencies from a signal, which can be divided into two classes: passive (made of capacitors, resistors, inductors) and active (involving an amplifier)

Figure 3C shows a miniature bandpass filter, model 8 MB10 100/10- PN/PN-1 of the Microwave Filter Company's MB series; they use high-quality components for narrow- and wide-band filter applications in the range 0.5-500MHz.

The bandpass filter is by far the most common filter used in MW and RF applications. The frequency range passed by a bandpass filter is determined by the specification for calculating the "resonant" or "centre frequency" (f_r) point where the output gain is at its maximum or peak value:

$$f_r = \sqrt{f_L} \times f_H$$

Here, f_L is the lower -3dB cutoff frequency point, and f_H is the upper -3db cutoff frequency point. This peak value is not the arithmetic average of the upper and lower -3dB cutoff points as one might expect, but the "geometric" or mean value.

Bandstop Or Bandreject Filters

Bandstop, band-reject or band-elemination (notch) filters are tuned circuits that prevent passage of signals within a specified band of frequencies. The specified frequency is the centre frequency, with performance specifications that include bandwidth, ripple, insertion loss and voltage standing-wave ratio.

Bandwidth is the range of frequencies that RF band-reject filters block with maximum attenuation. Ripple is the peak-to-peak variation of the passband response, and insertion loss is the total RF power transmission loss resulting from the insertion of a device into a transmission line.

Figure 4B (left) shows the amplitude spectrum of a

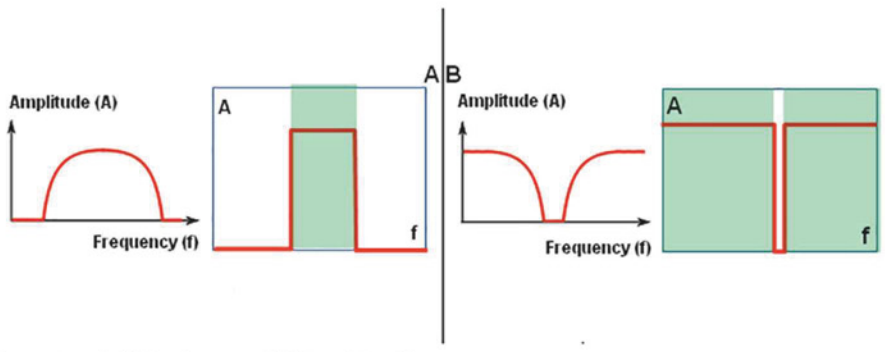

Figure 4: Amplitude spectra of: (A) bandpass; and (B) bandstop filters

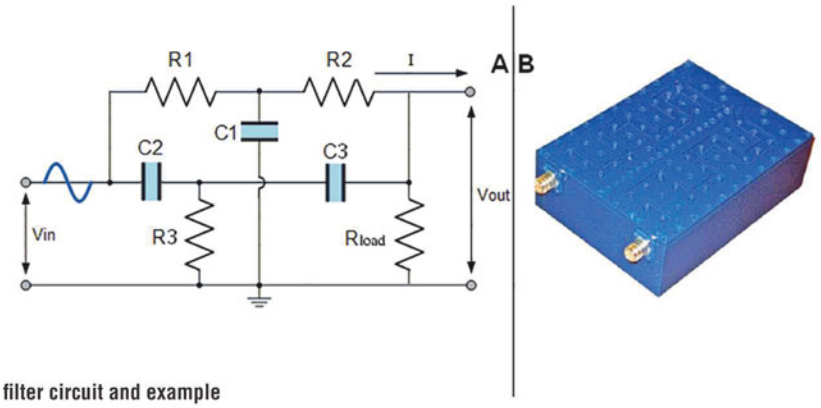

Figure 5: Bandstop filter circuit and example

bandstop filter with its parameters.

In signal processing, bandstop filters pass most frequencies unaltered, but attenuate those in a specific range to very low levels, see Figure 5A. The filter can be made of highpass and lowpass filters, just like the bandpass design, except this time the two sections are connected in parallel rather than series.

Figure 5B shows the small package size of a VHF-band bandstop filter from Reactel that rejects all frequencies between 240MHz and 270MHz by 60dB.

The lowpass section of a bandstop filter comprises R_1, R_2 and C_1 in a "T" configuration, and the highpass section comprises C_2, C_3 and R_3 also in a "T" configuration. Together, this arrangement is commonly known as a "Twin-T" filter, giving sharp response when the component values are chosen in the following ratios:

$$\mathbf{R_1 = R_2 = 2(R_3) \text{ and } C_2 = C_3\ (0.5)\ C_1}$$

Given these component ratios, the frequency of maximum rejection, known as "notch frequency" (NF) can be calculated as follows:

$$\mathbf{f_{NF} = 1/4\pi R_3 C_3}$$

There are different mounting styles for RF bandstop filters, which use several types of connectors. Bandstop filters are used as telephone line noise reducers, in digital image processing and in many power amplification applications, such as electric guitars. They are also very useful in communications electronics for eliminating certain harmonics in signals and reducing interference.

Highpass Filters

A highpass filter allows high frequencies and rejects low ones, see Figure 6A. In this circuit arrangement, the reactance of the capacitor is very high at low frequencies; the capacitor acts like an open circuit, blocking any input signals until the cutoff frequency (f_C) is reached. Above f_C the reactance of the capacitor decreases sufficiently to act like a short circuit, allowing the entire input signal to pass directly to the output.

The f_C for a first-order highpass filter can be determined using the same equation as for a lowpass filter, while the equations for gain (A_V) and phase shift (φ) are modified slightly to account for the positive phase angle, as shown here:

$$\mathbf{A_V = V_{out}/V_{in};\ f_C = 1/4\pi RC;}$$

$$\mathbf{\varphi = \arctan 1/4\pi fRC}$$

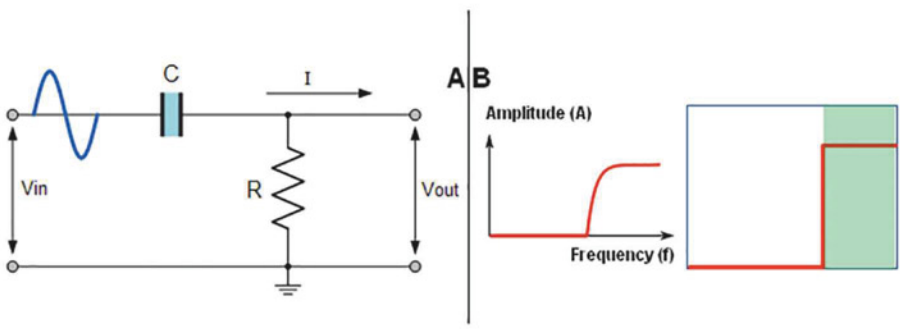

Figure 6: Highpass filter circuit and amplitude

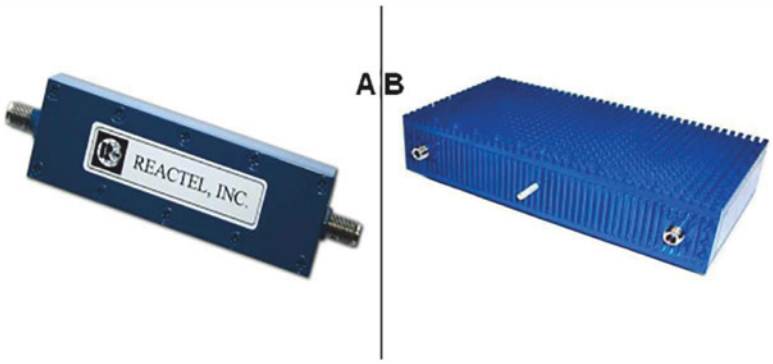

Figure 7: (A) Highpass; and (B) lowpass filter

This way, the signal is attenuated or damped at low frequencies with increasing output, whereas the lowpass filter only allows signals to pass below its cutoff frequency (f_C).

The actual amount of attenuation at each frequency varies from filter to filter. A highpass filter is usually modeled as a linear time-invariant system. It is sometimes called a low-cut filter or bass-cut filter.

Highpass filters have many uses, including blocking DC from circuits sensitive to non-zero average voltages, or RF devices. A highpass filter is often used to suppress acquisition noise.

Figure 6B (left) shows the amplitude spectrum of a highpass filter, with its parameters.

Figure 7A shows a wideband highpass filter with a passband of 18-40GHz, made by Reactel. This tiny unit is perfect for portable or "hi-rel" applications.

Lowpass Filters

Lowpass filters are the opposite of highpass filters, allowing low frequency signals and attenuating or reducing the amplitude of signals with frequencies higher than the cutoff frequency. In audio transmission applications they are also known as high-cut filters or treble-cut filters.

A simple passive RC lowpass filter can easily be made using a single resistor and a single capacitor in series, as shown in Figure 8A. In this arrangement the input signal is applied to the combination (resistor and capacitor in series) but the output signal (V_{out}) is taken across the capacitor only. This type of filter is generally known as a "first-order filter" or "one-pole filter", because there's only one reactive component in the circuit – the capacitor. Although this is an RC lowpass filter, it can also be called a frequency-variable voltage divider, using the following calculation of total resistance of the circuit (R_T) and the output voltage for two single resistors connected in series:

$$\mathbf{V_{out} = V_{in} \times R_2/R_1 + R_2, \text{ where } R_1 + R_2 = R_T}$$

Lowpass filters exist in many different forms, and are used in audio applications and anti-aliasing filters to condition signals prior to analog-to-digital conversion. They can also be used for smoothing data, as acoustic barriers, for blurring images and so on.

Figure 8B (left) shows the amplitude spectrum of a lowpass filter with its parameters. Figure 7B shows a high-power lowpass filter made by Reactel, which passes the HF band with rejections to 500MHz, all the while withstanding power levels of 1250W.

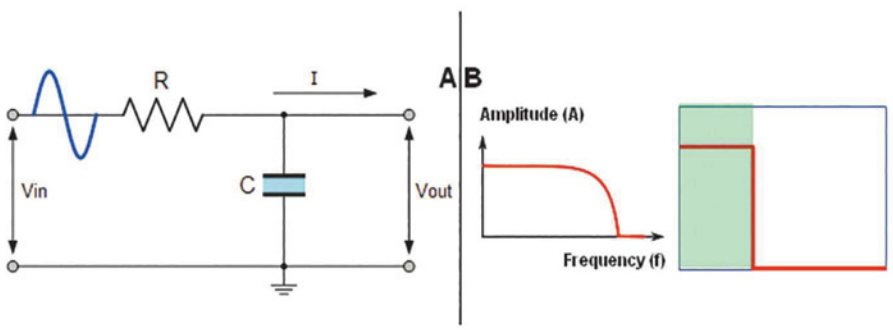

Figure 8: Lowpass filter circuit and parameters

THE DESIGN OF A RECTANGULAR ANTENNA FOR UHF RFID APPLICATIONS

K. THANAPAKKIAM, **J. S. MANDEEP** AND **M. T. ISLAM** FROM THE NATIONAL UNIVERSITY OF MALAYSIA PRESENT THE STRUCTURE, PROTOTYPE AND MEASUREMENTS OF A RECTANGULAR RADIATOR ANTENNA FOR UHF RFID APPLICATIONS

Radio frequency identification (RFID) is an automatic identification system based on electromagnetic (EM) waves. It is a means of electronic information transmission/data acquisition, using reflected modulation as the main communications method.

RFID technology is used in many sectors, including logistics, inventory management, security, transportation, defence, medicine and so on.

RFID System

A typical RFID system consists of a reader and a tag. The tag gets its power from the readar's modulated electromagnetic signal.

The standard RFID frequencies are in the ISM band (2.4-2.5GHz), ultra high frequency (UHF) band (860-960MHz) and high frequency (HF) band (13.56MHz). In addition, RFID is used at different frequencies in different countries, such as 950-956MHz in some parts of Asia, 902-928MHz in North and South America, and 866-869MHz in Europe.

HF-bandwidth RFID has the disadvantage of very narrow antenna recognition, but it's frequently used for short-distance reading applications.

For wireless communications, especially for long distance reads, UHF-band RFID is more suitable and therefore more commonly used.

Typically, for the reader, and especially in circular polarization antennas, the original signal is split into two signals with a phase difference of $\lambda/2$, which increases the antenna's radiation efficiency. To generate a wide bandwidth, a patch antenna structure is better, especially when designed with asymmetric feeds from a rectangular patch.

Antenna Structure

We designed a wideband rectangle radiator antenna for UHF RFID applications with a modified printed antenna. The design consists of two rectangular radiator patches symmetrically placed along the x axis. The rectangular patches are connected to a feedline, and a circular slot is made in each for improved return loss, S11. The radius and location of the circular slots are adjusted on both sides to achieve UHF RFID wideband operation. The partial ground radiator also plays an important role in improving the return loss performance in these applications.

Our antenna design was simulated at three stages to investigate its performance, making adjustments at each stage to reach the desired specifications, such as resonant frequency.

We printed a 130mm x 66mm x 1.575mm antenna on a 0.035mm-thick substrate, with a partial ground plate of 130mm x 10mm on the other side (see Figures 6a and 6b). It was designed so the waveguide feed line has impedance of 50Ω. The substrate is made of TLC 30 (TACONIC) material with a dielectric constant (ε_r) of 3.

Top Rectangle Radiator With Circular Slot

Figure 1a and b show the geometry of the circular slot, and Figure 1c shows the antenna's reflection coefficient. The design consists of a larger single rectangular radiator patch of 78mm x 31mm, attached to a smaller patch of 27mm x 6mm.

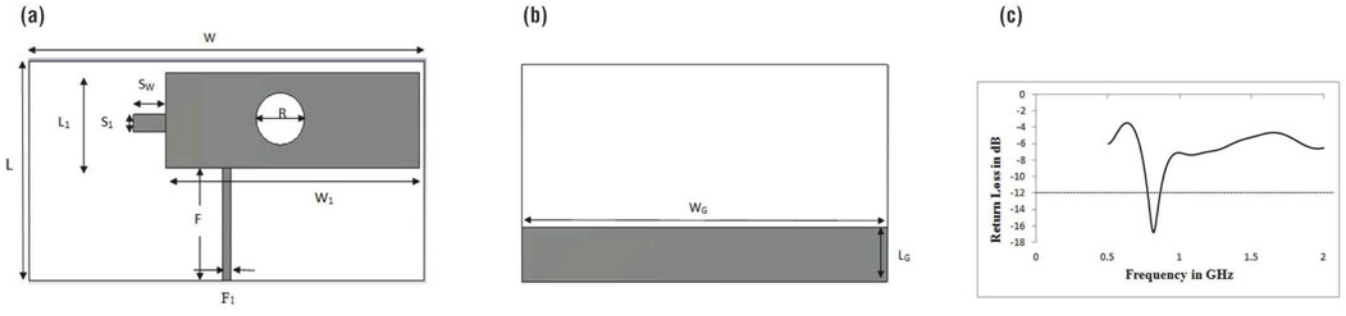

Figure 1: The proposed antenna with circular slot: (a) front view; (b) back view; and (c) return loss

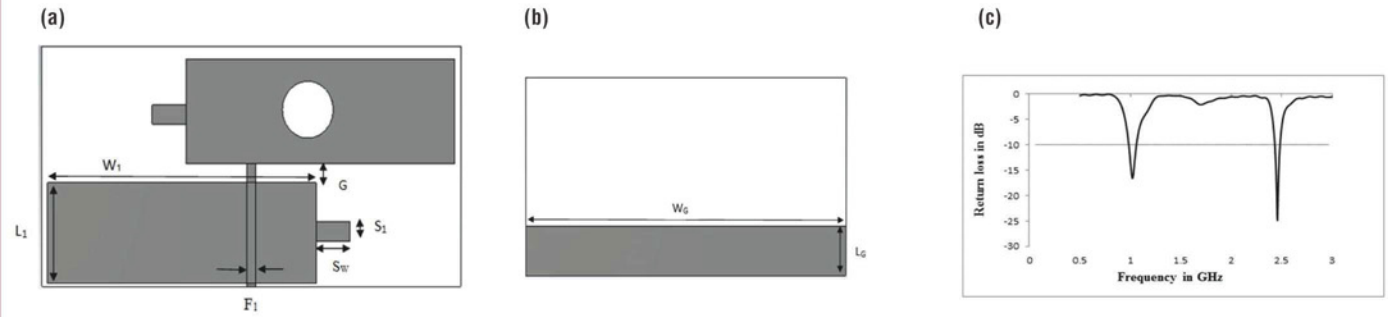

Figure 2: (a) Front view, (b) back view and (c) return loss of the proposed antenna with rectangular radiator

The circular slot inside the rectangular radiator is 9mm in radius, which generates the lower UHF frequency of 928MHz and return loss of 16.76dB (see Figure 1c). The upper frequency, however, is not generated, so for that a different rectangular radiator patch is added (see Figure 2a).

A suitable antenna shape and size are needed to achieve a good performance for UHF RFID applications, so the second patch helps with the resonant frequency, which now is 0.925GHz at 2.295GHz (see Figure 2c). However, this frequency is yet to be improved to reach the required 2.45GHz level. Figure 2b shows the back of the antenna.

To generate the required resonant frequency of 2.45GHz, a circular slot is added to the radiator patch, as shown in Figure 3a. When this is fabricated and simulated, the upper frequency and return loss are improved. Two radiator patches are interconnected by a feed line, 3mm wide x 33mm long.

Figure 3b shows the partial ground of the modified structure. The top radiator creates the lower frequency of 0.925GHz and the circular slot generates the return loss of 27.06dB. Similarly, the bottom radiator creates 2.45GHz and the circular slot generates a return loss S11 of 29.95dB, as shown in Figure 7, meeting the requirements of UHF RFID applications.

Performance And Analysis

Figure 4 shows the simulation results of our antenna's reflection coefficient with varying radii (R) of the circular slots, in both rectangle radiators. The antenna was tested with circular slot radii of 6mm, 7mm, 8mm and 9mm. This revealed that as the radius increases the return loss of the lower frequency 0.925GHz increases and the upper frequency 2.45GHz decreases. Therefore, 9mm is accepted as a suitable radius for the proposed antenna's circular slot.

Similarly, we performed a simulation with different gap widths (G) between the top and bottom of the rectangular radiators, for 4mm, 6mm and 8mm, as shown in Figure 5. The return loss and bandwidth at 2.45GHz remained unchanged. This could be due to the intrinsic properties of the TACONIC substrate and its dielectric constant. However, for 0.925GHz, as the gap width decreases so does the return loss, so we chose the size of the gap to be 6mm for our design.

We created a prototype to verify the proposed antenna, as shown in Figures 6a and 6b. The S-parameter was analyzed using a Rhode & Schwarz network analyzer ZVL-30. The optimal antenna parameters are shown in Table 1.

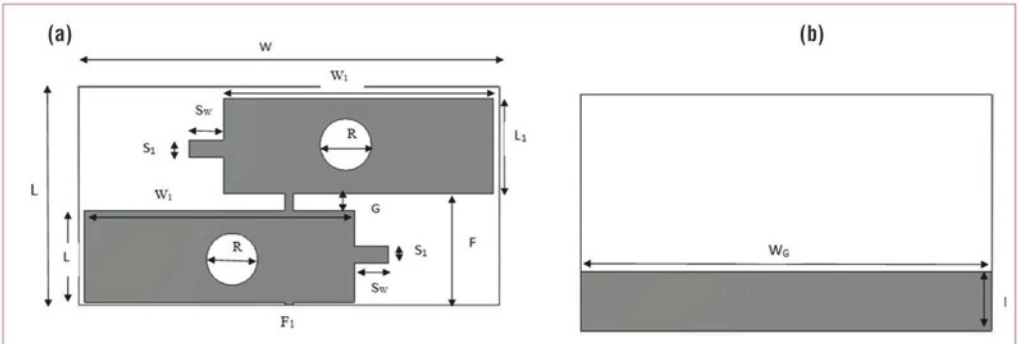

Figure 3: Proposed antenna with circular slot on the patch: (a) front view; (b) back view

Parameter	Label	Dimension (mm) x, y
Radiator Length Top & Bottom	L_1	31
Radiator Width Top & Bottom	W_1	78
Gap	G	6
Slot Top & Bottom	S_l S_w	27 6
Circle Top & Bottom	R	18
Feed line	F	3 x 33
Ground	W_g L_g	130 10
Substrate		130 x 66

Table 1: Antenna's optimized values

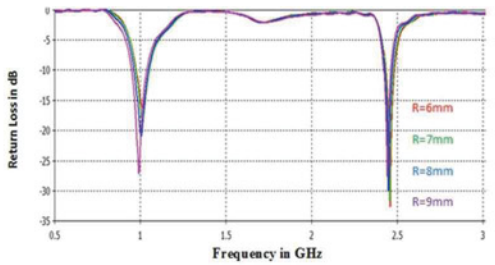

Figure 4: Simulated reflection coefficient for various radii (R)

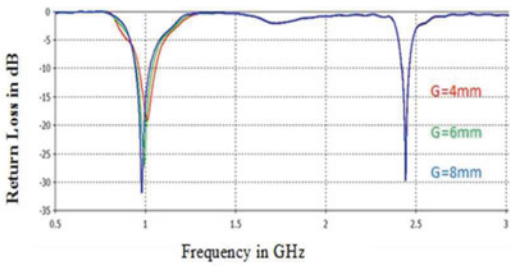

Figure 5: Simulated reflection coefficient for various gaps (G)

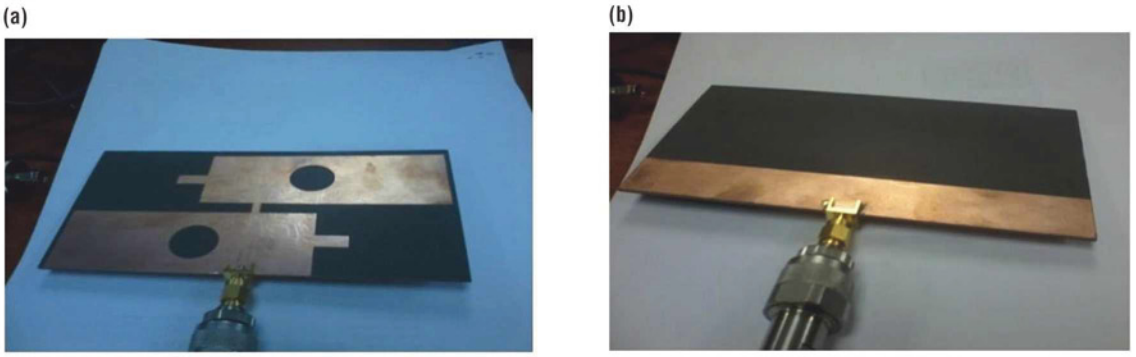

Figure 6: Fabricated antenna's: (a) front view; (b) back view

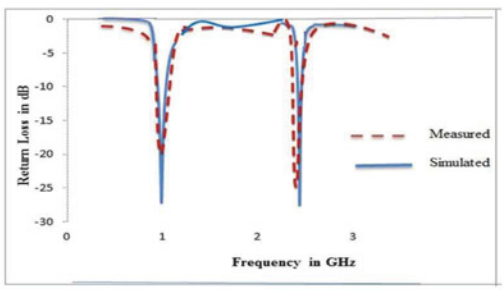

Figure 7: Simulated (solid line) and measured (dashed line) S11 for our proposed rectangular radiator antenna

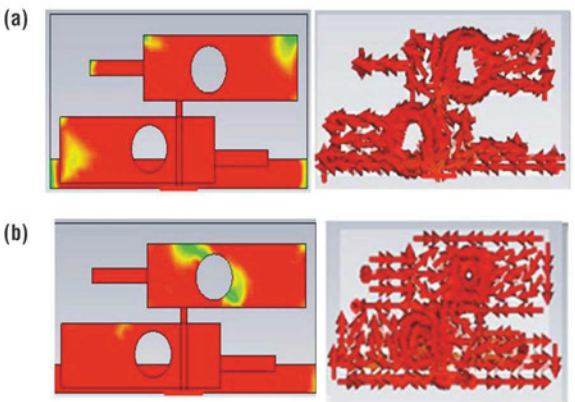

Figure 8: Surface current and current distribution for the designed rectangular radiator antenna at: (a) 0.927GHz; (b) 2.45GHz

The antenna's performance was determined using commercial simulation software called CST Microwave Studio; see the measured and simulated performances in Figure 7. The two results agree very well, so we conclude that the main parameters influencing the resonant frequency are the locations of the circular slots, on the top and bottom rectangular radiators, and the location of the radiator patches.

Current distributions usually give an insight into the physical behaviour of the antenna. Figure 8 shows the antenna's surface current distribution at 0.927GHz and 2.45GHz. Note that the maximum currents are focused at the circular slots of both rectangular radiators and that current is uniformly distributed in the radiating element. However, there is a lack of current on the surface of the radiating elements, which could be due to the electromagnetic characteristics of the antenna design and the current distribution at the resonant frequencies.

Radiation Patters

Based on the antenna's orientation in relation to the axes in Figure 9, the xz plane is the E plane, whilst the yz plane represents the H plane. The antenna's radiation patterns in the E and H planes are measured at frequencies close to the resonant frequencies.

RELEC ELECTRONICS LTD

Trying to keep a low profile?

Ranging from 40W to 112.5W with convection cooling and up to 225W with forced air cooling. Relec Electronics has a range of open frame ac dc power supplies on a 4" x 2" footprint with a height profile of just 25.4mm for those designs where a low profile is critical. All feature high efficiency with low standby power consumption and a universal ac input. Single fixed outputs range from 12 to 48Vdc on the lower power units and 12 to 58Vdc on the 112.5/225W unit.

Approved to IEC, EN, UL 60950-1 2nd edition, class II safety standards, the 40W & 60W PSU's have an optional function ground enabling them to meet class I when this is connected. Hold up time is between 10 and 16ms; the outputs are fully protected against over voltage and short circuits.

These power supplies are ideally suited for telecom, datacom and a wide range of industrial applications. For further information on the 40W **MPE-S040**, 60W **MPE-T060** or 112.5/225W **ABC225** series, view the Relec website or contact us directly.

Design solutions for design engineers

Relec Electronics Ltd
Tel: 01929 555800
e-mail: sales@relec.co.uk

www.relec.co.uk

RIGOL
Beyond Measure

Typical Rigol:
Rigol extends their RF product solutions
High End Performance for Best Price

DSG815 and DSG830 NEW!
RF Signalgenerators

- 9kHz to 1,5GHz or 9kHz to 3GHz max. Frequency
- Ampitude accuracy: < 0,5dB (typ.)
- Phase noise: -105dBc/Hz (typ.)

DSA832 (-TG) and DSA875 (-TG)
High End Spectrum Analyzers

- 9kHz to 3,2 or 7,5GHz max. Frequency
- Min. -161dBm Displayed Average Noise Level (DANL)
- Min. -98dBc/Hz @10kHz Offset Phase Noise

DSG3030 and DSG3060
RF Signal Source

- 9kHz to 3,0 or 6,0GHz max. Frequency
- Ampitude accuracy: < 0,5dB (typ.)
- Amplitude range: -130dBm to +13dBm
- Phase noise: > -110dBc/Hz@20kHz (typ.)

Options: IQ Modulation and Baseband input/output, **PC Software Ultra IQ Station** (generate and edit user defined IQ modulation)

RIGOL Technologies EU GmbH
Phone +49 89 8941895-0
info-europe@rigol.com
DISTRIBUTION PARTNERS:
www.rigol.eu/sales

The radiation patterns are normalized by taking the highest value as a reference. It is observed that in both E and H planes the co-polarized field is omnidirectional at lower frequencies and retains good omnidirectionality as frequency increases. In the E plane the cross-polarized fields are much weaker than the co-polarized fields, especially at lower frequencies. Although some harmonics are introduced at higher frequencies, the proposed antenna exhibits essentially symmetrical omnidirectional radiation.

The measured and simulated peak gain plot of the designed antenna is shown in Figure 10. For the lower band at 0.925GHz the gain is about 6.5dBi; the higher achievable gain is 7.4dBi at 2.45GHz.

Figure 11 shows a comparison between the simulated and measured voltage standing wave ratio (VSWR) versus the frequency curve of the designed antenna. It can be seen that VSWR is less than 2 throughout.

All measurement results confirm that our antenna design achieves good performances, making it suitable for UHF RFID reader or tag applications. ●

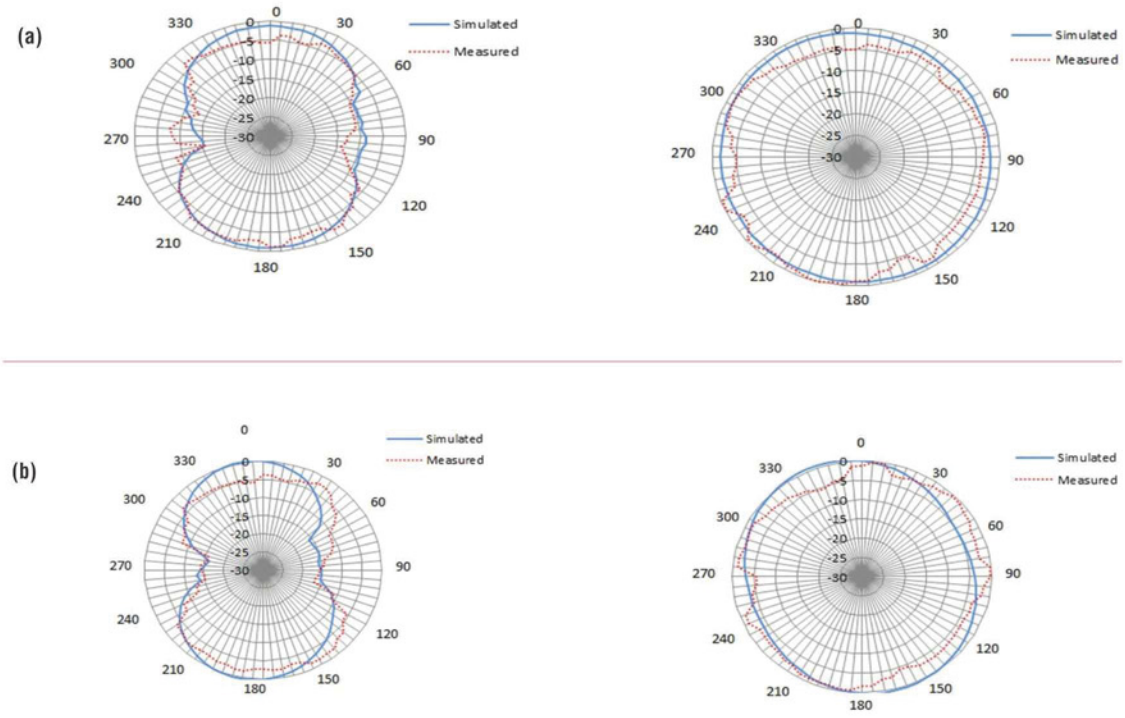

Figure 9: Measured versus simulated radiation patterns for the E- and H-planes at: (a) 0.925GHz; (b) 2.45GHz

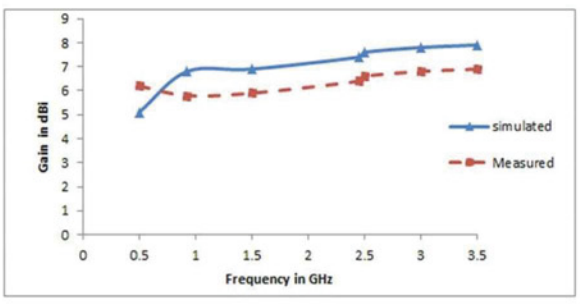

Figure 10 : Measured and simulated gain in dBi for different frequencies

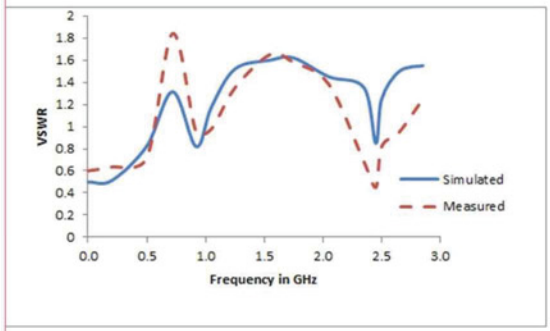

Figure 11: Comparison between simulated and measured voltage standing wave ratio (VSWR) versus frequency of our antenna design

RADIOMETRIX

www.radiometrix.com

Frequency Programmable Narrow Band Transmitter

New range of highly flexible, frequency programmable, RF power adjustable radios.

True Narrow Band FM performance, available on user/factory programmable custom frequencies between 425MHz & 470MHz. Matching receiver available.

VISIT http://radiometrix.com/content/ntx2b

CALL +44 (0)20 8909 9595 *REAL RADIOS FOR REAL APPLICATIONS*

M. R. I. FARUQUE, M. M. ISLAM, M. T. ISLAM AND **M. SAMSUZZAMAN** FROM UNIVERSITI KEBANGSAAN IN MALAYSIA CONVERT AN ULTRA-WIDEBAND ANTENNA INTO A SUPER-WIDEBAND ANTENNA BY PLACING A PARASITIC ELEMENT ON THE GROUND PLANE. THE ANTENNA THEN RADIATES IN A NEAR OMNIDIRECTIONAL MANNER

ULTRA-WIDEBAND TO SUPER-WIDEBAND ANTENNA CONVERSION USING PARASITIC ELEMENTS

By releasing the 3.1-10.6GHz frequency band for unlicensed radio communication, the Federal Communications Commission (FCC) opened new opportunities in the field of short-distance wireless communication. So far, the ultra-wideband (UWB) antenna has dominated ultra-wide band communication, owing to various merits such as high data rate, low multi-path interference, large bandwidth, small emission power, suitability for remote sensing applications, low cost, and so on. Recently, in our work, various super-wideband (SWB) antennas have taken centre stage in different shapes.

Monopole antennas are used widely in various applications, since they meet UWB demands with right gain and bandwidth. However, on the negative side, at lower frequencies (2-2.5GHz) their input impedance is not matched properly, and at 35 × 77mm² they are too large. A monopole antenna for super wideband (SWB) applications offers high peak gain but is still too large.

> The SWB antenna has the PE placed on the ground plane to generate a super-wide bandwidth, from 3.08GHz to over 20GHz

Academics proposed an SWB antenna with printed patch and tapered feed region; however, its input impedance is mismatched at 18-19GHz, which creates variable group delay; also, at 40 × 30mm² it is also too large.

In our study we recommend a UWB-to-SWB antenna conversion with a parasitic element (PE) to achieve near omnidirectional radiation and smooth current distribution. The SWB antenna has the PE placed on the ground plane to generate a super-wide bandwidth, from 3.08GHz to over 20GHz.

The antenna is simple and easy to make.

Antenna Structure

Figure 1 shows the SWB antenna's design. The antenna is made of a parasitic element on the ground plane and a circular patch. The antenna has been printed on both sides of a dielectric FR4 substrate 1.6mm thick, and with permittivity of 4.6 and loss tangent of 0.02; its overall dimensions are 25 × 33mm². See Table 1 for its optimal parameter values.

The antenna patch is of circular design, and some modifications were made on the ground plane to improve its performance. To enhance the impedance bandwidth, we applied different measures, see Figures 1c-1e, which include:

- Adding a rectangular slot at around 30° angle, length l1 and width 0.87mm on the upper part of the ground plane as a parasitic element.
- Embedding a slot horizontally with length w1 and 1mm width.
- Attaching a 33° slot with length l2 and 1mm width.
- Adding a 30° slot with 10.1mm length and 1.1mm width.

By choosing the optimized parameters of Table 1, the proposed SWB antenna can be tuned for SWB applications.

Results And Discussion

We built the SWB antenna with the parasitic element, simulated it and measured the results. Its input impedance and radiation properties are presented and explained here.

High frequency structural simulator (HFSS) is applied for

Para	L_{sub}	W_{sub}	H_{sub}	l_1	l_2	g_1	g_2	g_3	d	w_1
mm	25	33	1.6	11	8.7	.5	3	1.1	1.23	11.05

Table 1: Optimized dimensions of the proposed SWB antenna

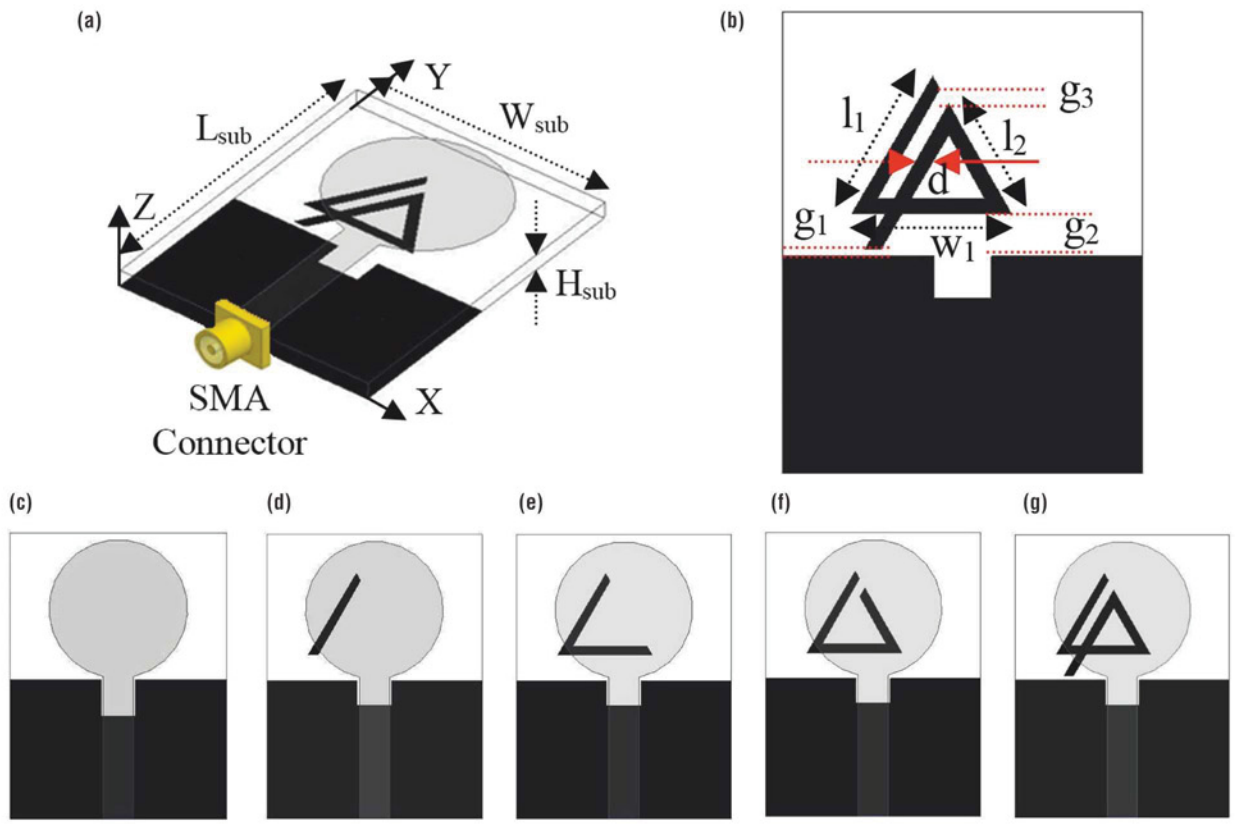

Figure 1: Geometry of the proposed antenna: (a) side view; (b) with parasitic elements, bottom view; (c) conventional UWB antenna; (d) antenna 1; (e) antenna 2; (f) antenna 3; and (g) the proposed SWB antenna

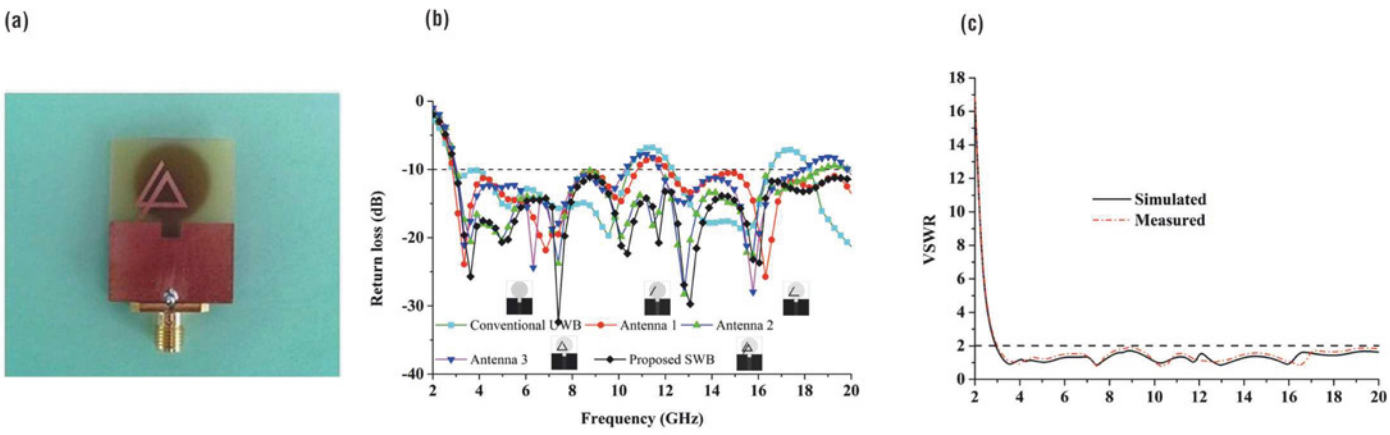

Figure 2: (a) Photograph of the proposed SWB antenna; (b) simulated return losses of the various antennas; (c) measured and simulated VSWR of the proposed SWB antenna

achieving simulation results. The fabricated prototype is shown in Figure 2a. Figure 2b shows the effects of parasitic structures on the impedance matching compared with conventional UWB antennas, as well as the proposed SWB antenna. It is observed that by implementing the parasitic element structure on the ground plane the antenna's impedance bandwidth improves, making it suitable for SWB applications.

Figure 2c shows the measured and simulated voltage standing

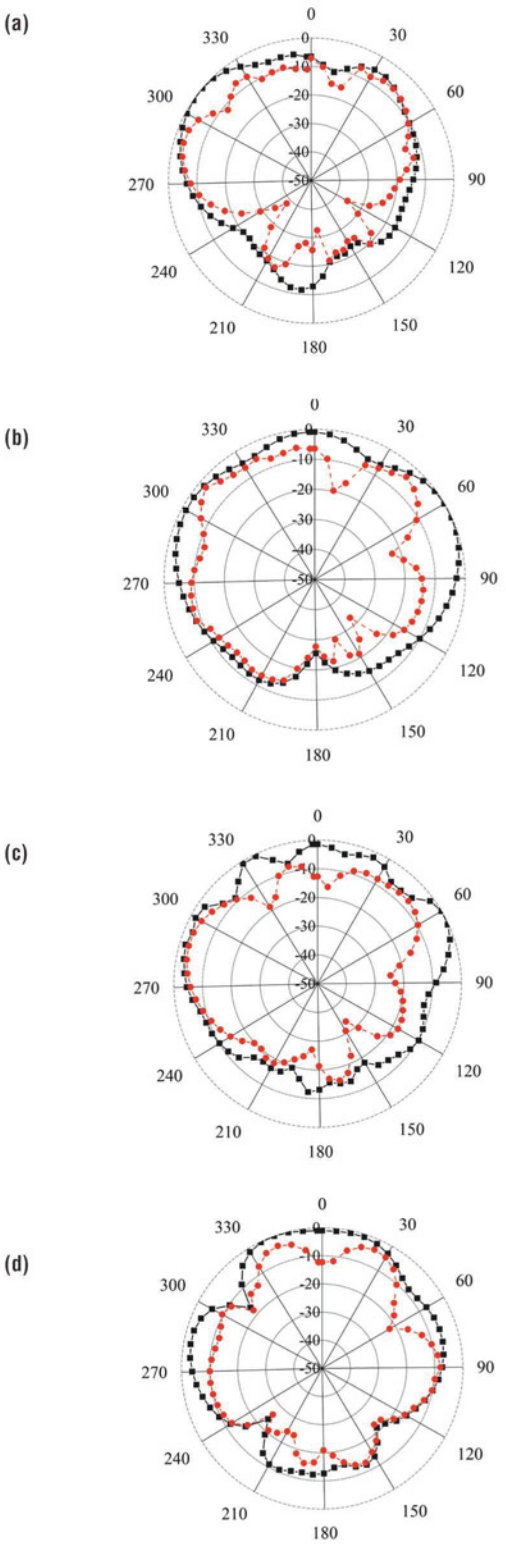

Figure 3: Measured radiation patterns of the proposed SWB antenna on: (a) the E-plane at 13GHz; (b) H-plane at 13GHz; (c) E-plane at 16GHz; (d) H-plane at 16GHz

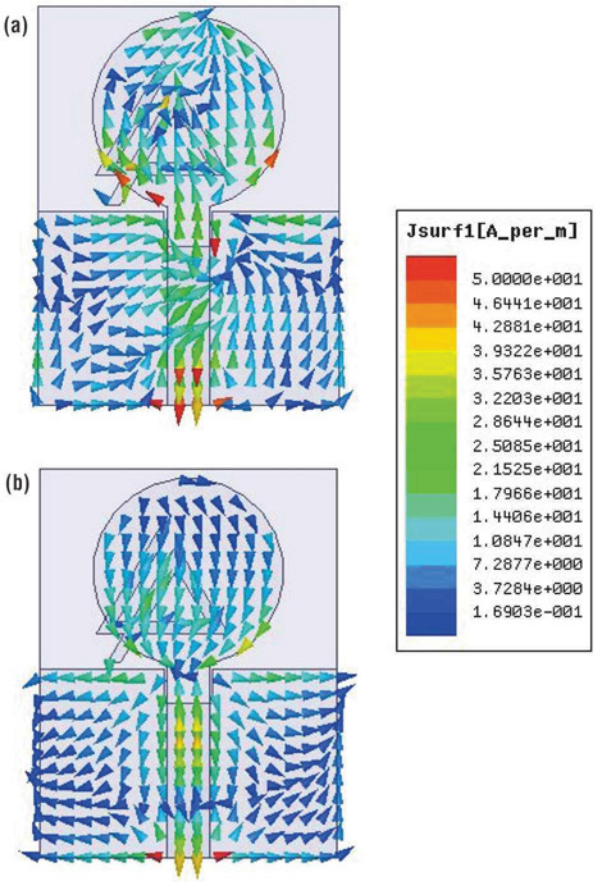

Figure 4: Surface current distribution of the proposed SWB antenna at: (a) 3.5GHz; (b) 7.5GHz

wave ratio (VSWR) properties of the proposed SWB antenna. The antenna exhibits a wide frequency bandwidth, from 3.08GHz to over 20GHz for VSWR < 2.

Figure 3 shows the SWB antenna's measured radiation pattern at 13GHz and 16GHz with co-polarization and cross-polarization, where the x-z plane is considered H-plane and the y-z plane E-plane.The co-polarization dimension is greater than the cross-polarization dimension on both the H-plane and E-plane at the resonances of 13GHz and 16GHz respectively.

It is observed that the proposed SWB antenna exhibits better broadside radiation features, a considerable front-to-back ratio with low cross-polarization, which leads to symmetric and nearly omnidirectional radiation pattern.

Optimized design parameters are applied to achieve the required surface current distribution. Figure 4 shows the surface current distribution at 3.5GHz and 7.5GHz, neighbouring the parasitic element on the ground plane and the feed line. The flows of the current in the parasitic element are inverse to the current flows in the outward edges of the radiator patch and ground. Consequently, the entire effective radiations are reduced enough or cancelled out completely, and a super-wideband is generated. ●

NOVEL HANDHELD RFID READER ANTENNA FOR ENHANCED SENSITIVITY

BO WANG, YIQI ZHUANG, XIAOMING LI AND **WEIFENG LIU** PRESENT A COMPACT ANTENNA WITH TWO PORTS TO TRANSMIT AND RECEIVE SIGNALS SEPARATELY

Handheld RFID readers until now used a single port for receiving and transmitting signals. Here, we recommend a two-port version which enhances their receive sensitivity.

Our design uses an aperture-coupled patch structure that occupies less space. To improve isolation between ports, we added two stubs in the T-shaped microstrip feed lines. The antenna has two symmetric U-shape apertures etched onto the ground plane to excite two orthogonal modes for dual-polarized operation.

RFID System Structure

An RFID system consists of a tag and a reader that exchange data using a continuous wave (CW).

It is not easy to achieve high isolation between the receive (Rx) and transmit (Tx) ports in dual-polarized antennas, so the Rx port receives weak signals that backscatter from the tag, and

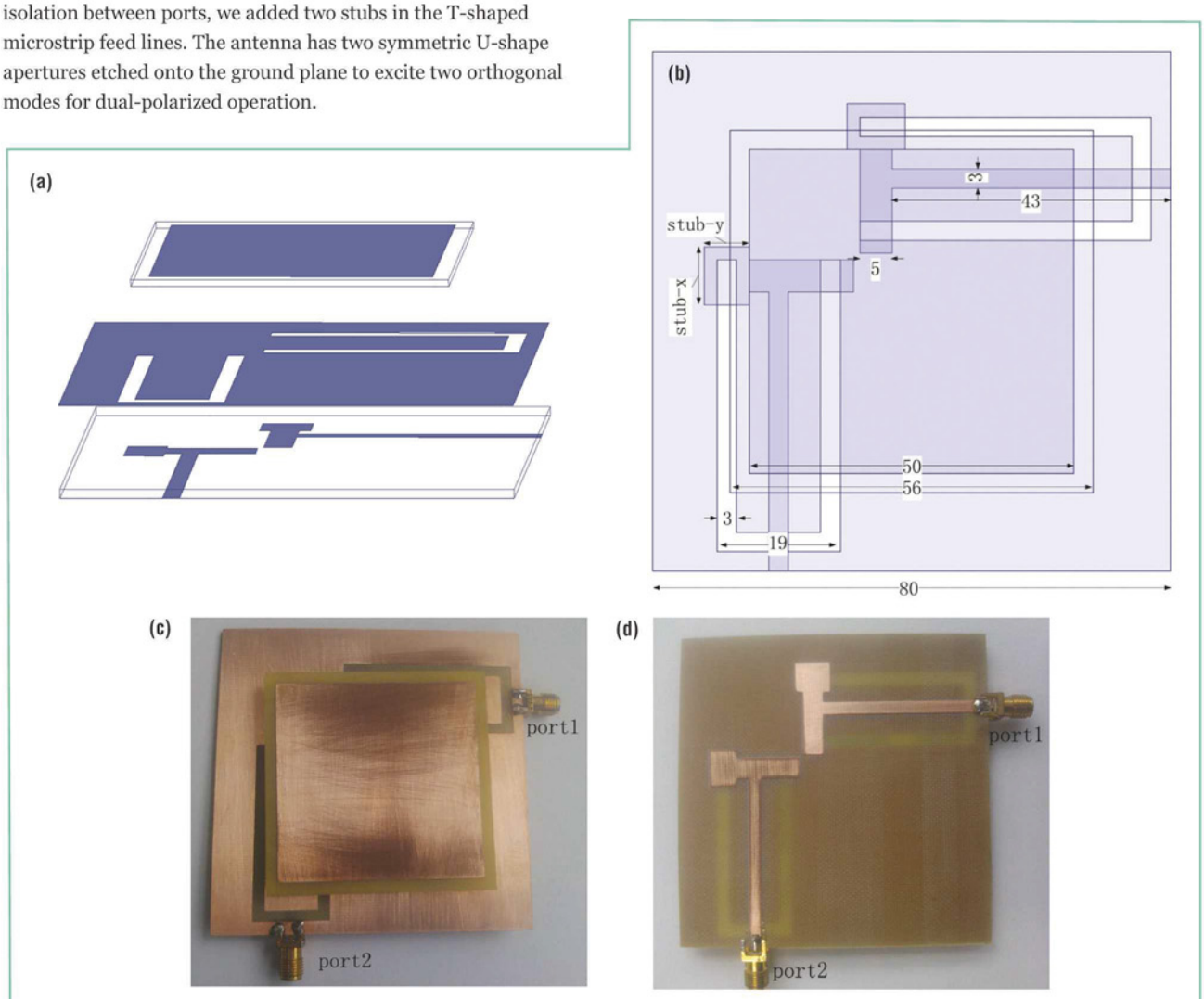

Figure 1: (a) Side view of the proposed antenna; (b) antenna configuration; (c) fabricated antenna's top view; (d) bottom view

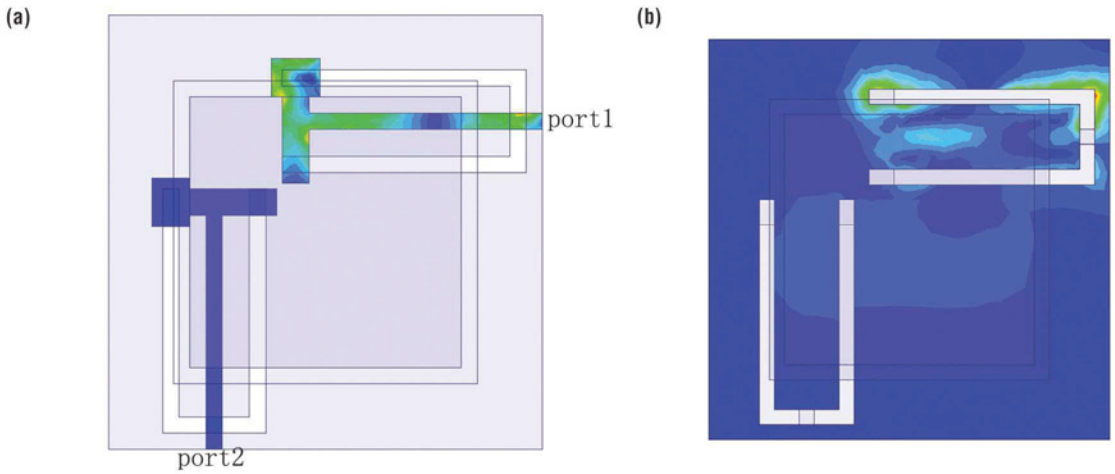

Figure 2: Surface current distribution of proposed antenna on: (a) the feed lines; (b) ground plane

these usually couple to the Tx port, decreasing reader sensitivity. The interference between the two ports plays a vital role in the design's performance.

Another challenge in designing antennas is the necessary size limitations. The antenna's compactness is of critical importance, especially since it will be part of a handheld RFID reader – unlike in stationary readers, where bigger antenna sizes can be easily accommodated. In a handheld RFID reader, the antenna should be around 100mm in length and width, and around 10mm thick.

Dual-polarized non-handheld RFID reader antennas have until now been designed with a branch line coupler to minimize Tx and Rx coupling. The disadvantage of a directional coupler, however, is reduced receive power; the improvement in reader sensitivity is questionable.

Among the dual-polarized antenna designs, aperture-coupled microstrip patch antennas are the most suitable candidate for RFID applications. Aperture coupling is preferred to other feed configurations of a microstrip patch antenna due to its greater design flexibility, easier fabrication and lower cost.

In these designs, to gain high port isolation the thickness of the air substrate is increased, adding to their bulkier profile. Despite that, they are still not able to meet the isolation requirement of S21 < -25dB and impedance matching of RL < -10dB over the entire RFID ISM band (2.4GHz-2.48GHz).

This paper applies a U-slot to couple energy from the T-shaped feed lines to the square patch and stubs to increase isolation between the Rx and Tx ports. Meanwhile, the thickness of the air layer is reduced to only 4mm (0.032 wavelength). The proposed antenna not only occupies less space in a handheld RFID reader but also achieves the required isolation.

Antenna Design

The configuration of a dual-feed aperture-coupled square patch is shown in Figure 1b, with dimensions in millimeters. The design consists of two FR4 substrates with a dielectric constant of 4.4 and loss tangent of 0.02.

A single-layer substrate of 56mm × 56mm × 1.2mm is suspended 4mm above the 80mm × 80mm × 1.6mm double-layer substrate. A square patch 50mm × 50mm in is etched on top side of the single-layer substrate. Overall size of the proposed antenna is 80mm × 80mm × 6.8mm.

Two T-shape microstrip lines with stubs are fed by separate ports 1 and 2 on the bottom of the double-layer substrate, and the ground plane with U-slots is etched on top of it. The antenna uses a square microstrip patch antenna as radiator and U-shape coupling apertures on the antenna's ground plane to couple the microwave energy from the feed lines.

To improve impedance matching and isolation, we've added stubs at the end of the feed lines. Current concentrates in the stubs, thus introducing capacitive coupling to the square patch. This effectively increases the isolation and impedance matching of the antenna.

In most aperture-coupled patch antennas the feed lines' substrate is made of a thin, high-dielectric-constant substrate. The radiator is printed on thick, low-dielectric-constant substrate, needed to achieve a large bandwidth and good radiation efficiency. The two substrates in our antenna design are both FR4, with different thicknesses. In addition, spurious radiation from the feed lines is eliminated thanks to ground plane shielding, resulting in very low cross-polarization.

Coupling

To investigate the mechanism of mutual coupling between the two ports, current distribution in different layers under the patch have been simulated with port 1 excited and port 2 terminated. Our simulation is for 2.45GHz; see Figure 2.

Figure 2a shows that the microwave energy concentrates in the junction and stub of the T-shape feed line, and that the surface current flows along the feed line from port 1 to port 2, gradually attenuating. The current around port 2 is a lot weaker than around port 1.

Figure 2b shows that current concentrates in the specific

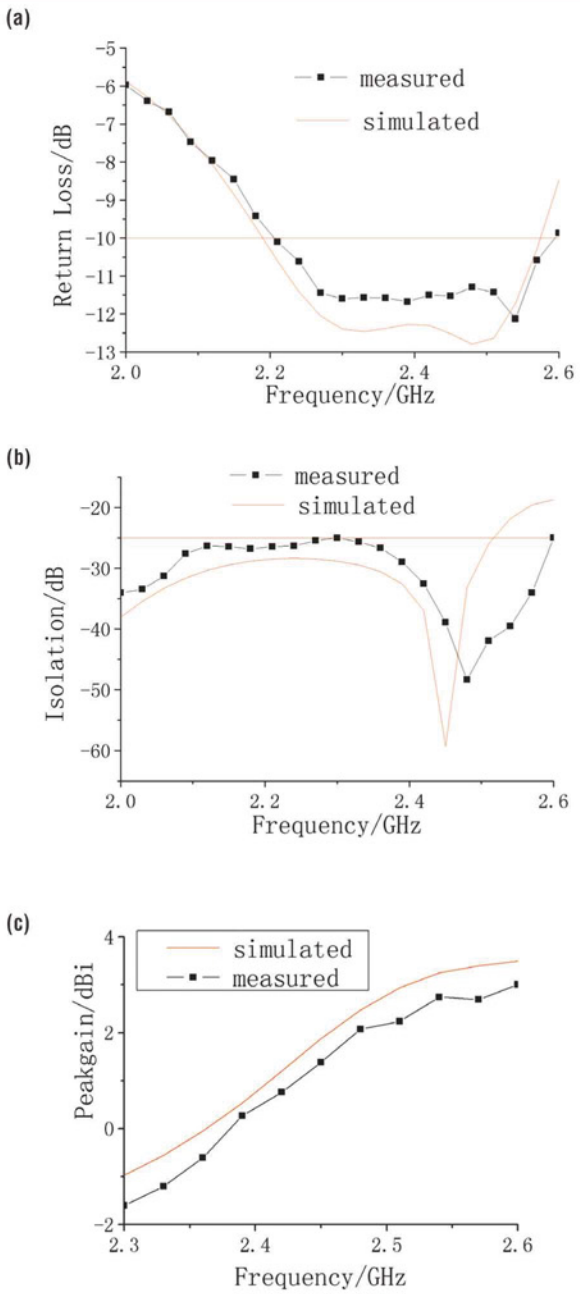

Figure 3: The proposed antenna's characteristics: (a) return loss; (b) isolation; (c) peak gain

region of the ground plane above the stub of the feed line, and that the end of the feed line without a stub has less current, confirming the stubs' effects.

Figure 2b also shows the current around the U-slot decreasing significantly, which can be attributed to impedance matching.

Figure 3a shows the simulated and measured return loss of the antenna. The simulated return loss is below -10dB over the frequency band of 2.19GHz to 2.58GHz, while the measured return loss bandwidth is 400MHz from 2.2GHz to 2.6GHz (the measured -25dB bandwidth of 2-2.6GHz is obtained with minimum -50dB at 2.48GHz, corresponding to a simulated bandwidth of 510MHz).

The simulated and measured peak gains are shown in Figure 3c. The antenna exhibits peak gain from 1.5-3.1dBi in the frequency band of 2.4-2.48GHz.

All three – measured and simulated return loss, isolation and peak gain – are in good agreement.

Antenna Optimization

Figure 4 shows the measured radiation patterns at 2.45GHz in the orthogonal XOZ (phi = 0°) and YOZ (phi = 90°) planes with angular step of 20°. The radiation pattern is bow-tie-shaped in the YOZ plane, but it's unidirectional in the XOZ plane.

Parameter simulations are carried out to provide antenna engineers with detailed information for antenna design and optimization. Stub lengths stub-x and stub-y are prime parameters that determine the amount of power concentrated in the stub and coupled to the radiating patch for purposes of impedance matching and isolation. One of these attributes varies independently, whereas the other is kept unchanged.

In our analysis, we used software high-frequency structure simulation (HFSS) based on the finite element method, which helps optimize antenna values to stub-x = 9mm and stub-y = 7mm.

Figures 5a and 5b show that the bandwidth of the return loss (< -10dB) and isolation (< -25dB) both increase with the decreasing length of stub-x. Figure 5a shows that both return loss bandwidth and resonant frequency decrease as the length of stub-x increases. It can also be seen that the isolation reduces dramatically as the length of stub-x increases, see Figure 5b. Minimum isolation with stub-x of 9mm is -60dB at 2.45GHz. Stub-x's length determines the strength of the coupling between the feed line and ground, so it has an impact on both return loss and isolation.

Figure 6 shows the effects of various dimensions of stub-y on return loss and isolation. The stub-y variations show a small effect on return loss, but a severe one on isolation. The bandwidths of return loss and isolation are almost the same, but an optimized value of stub-y of 7mm shows the best isolation in the range 2.4GHz-2.48GHz. ●

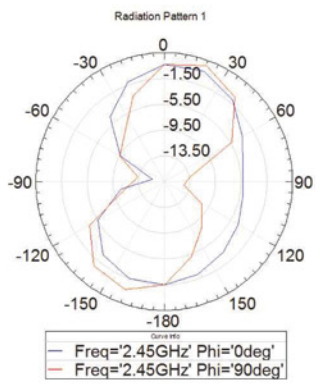

Figure 4: Measured radiation patterns of the proposed antenna at 2.45GHz

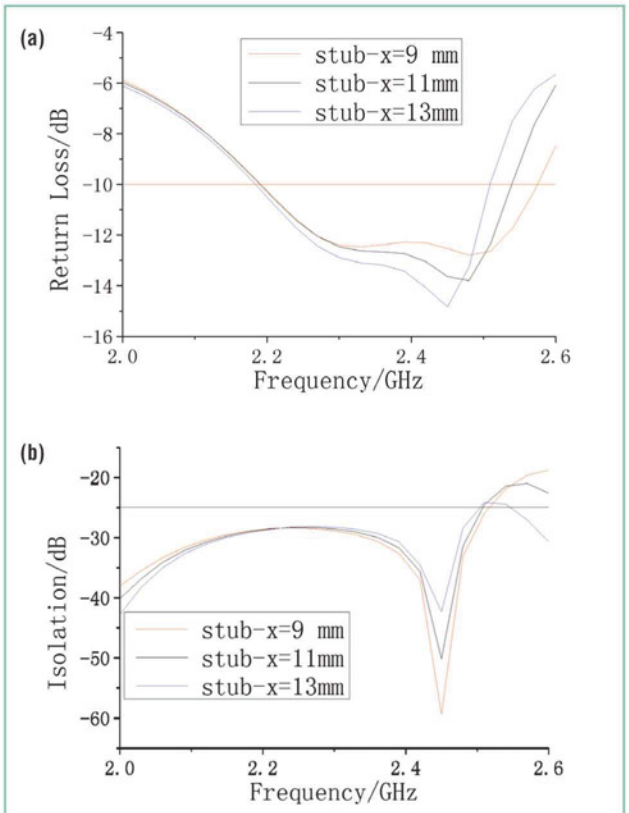

Figure 5: Antenna characteristics for different values of stub-x: (a) return loss; (b) isolation

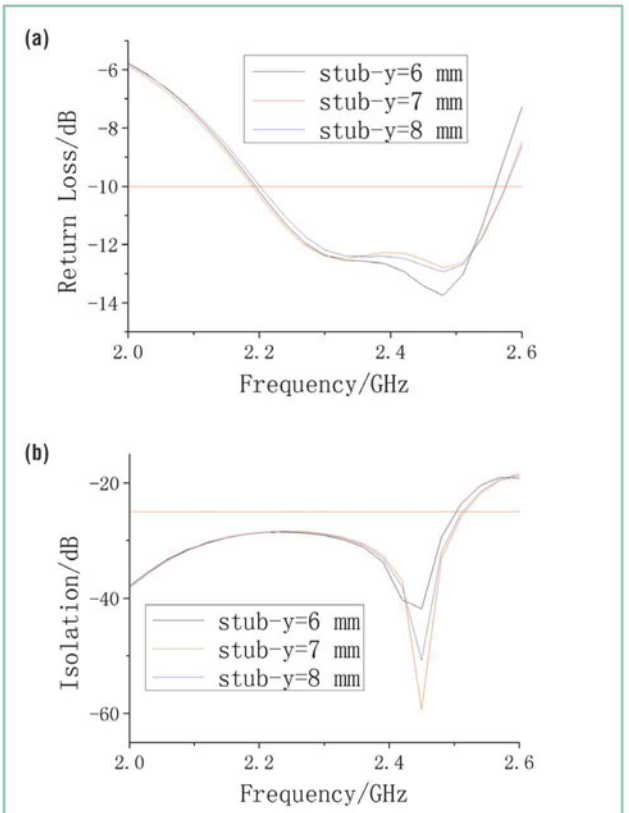

Figure 6: Antenna characteristics for different values of stub-y: (a) return loss; (b) isolation

EASING CONNECTIVITY FROM EDGE NODE TO CLOUD ANALYTICS

SIMON DUGGLEBY, MARKETING MANAGER FOR SEMICONDUCTORS AT RS COMPONENTS, GIVES A BRIEF INTRODUCTION TO THE INTEL EDISON PLATFORM AND THE EASE WITH WHICH AN IOT APPLICATION AND ASSOCIATED ANALYTICS DASHBOARD CAN BE MADE TO FUNCTION IN A MATTER OF MINUTES

As the pace to bring IoT-based devices to market quickens, so too does the need for comprehensive development and prototyping boards on which embedded developers can build their design. Not only should these boards ease the process of building and validating a design, but in many cases they should easily be integrated into the end product.

Intel recently announced the Edison module (Figure 1), aimed directly at such requirements. Comprising a postage-stamp-sized compute module (35.3mm x 25mm x 3.9mm) and with incorporated 802.11 a/b/g/n Wi-Fi connectivity and Bluetooth 4.0 support, there are two different breakout board options to host it. At its heart is an Intel system-on-a-chip (SoC) with an Intel Atom dual-core, dual-threaded CPU running at 500MHz and a 32-bit Intel Quark microcontroller running at 100MHz. Together with 1GB RAM, 4GB Flash and 40 configurable GPIO pins, this module easily satisfies the processing needs for most IoT designs.

Running at 1.8VDC, the Edison module is also well-positioned for use in battery-powered wearable designs. The SoC runs a pre-installed embedded Yocto-compliant Linux distribution that also includes Python, Node.js and a comprehensive software stack.

Getting Started

The breakout boards include a basic option that extends the 70-pin GPIO from module to host board, and provides power management. The second board uses all available I/O and provides an Arduino Uno R3 compatible shield headers and level shifters. An Intel Edison Arduino integrated development environment (IDE) port is available from the Intel website.

To introduce the Intel Edison we'll refer to the Intel Edison kit for Arduino board, as seen in Figure 2, which includes both the breakout board and an Intel Edison module.

Recommended starting place is the 'Edison Getting Started Guide', available on the Intel communities website, which provides detailed installation instructions for Windows, Mac and Linux, and a step-by-step guide to attaching the Edison module to the Arduino breakout board and connecting it to a Wi-Fi router.

> Intel provides the analytics dashboard for non-commercial applications; it is a very easy yet comprehensive platform which helps validate the design

It is important to "flash" the Edison module before continuing, which involves downloading the most current image, dragging it across to the Edison mounted drive, and then rebooting. The initial connection to Edison is made via USB and the GNU screen utility that presents a simple terminal window for the next stages of configuration.

Achieving a booting Edison and being able to log in as root are key first steps. Using the configure_edison setup utility, the device name and password can be entered, then selected and attached to a Wi-Fi router. Once this has been achieved, Edison should be rebooted and, hopefully, will then be seen on the local network.

Figure 1: Intel Edison module

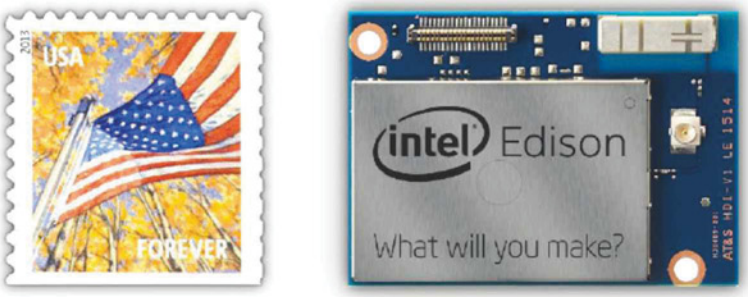

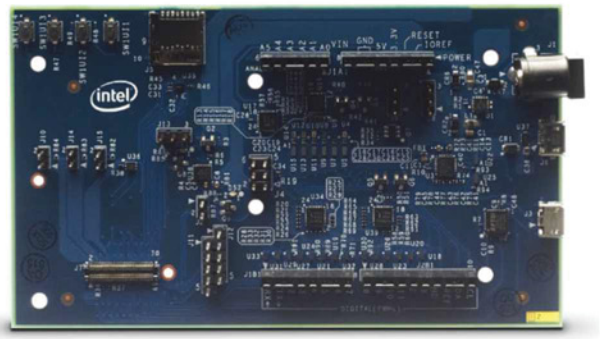

Figure 2: Intel Edison kit for Arduino

Figure 3: Success! Edison is found on the network

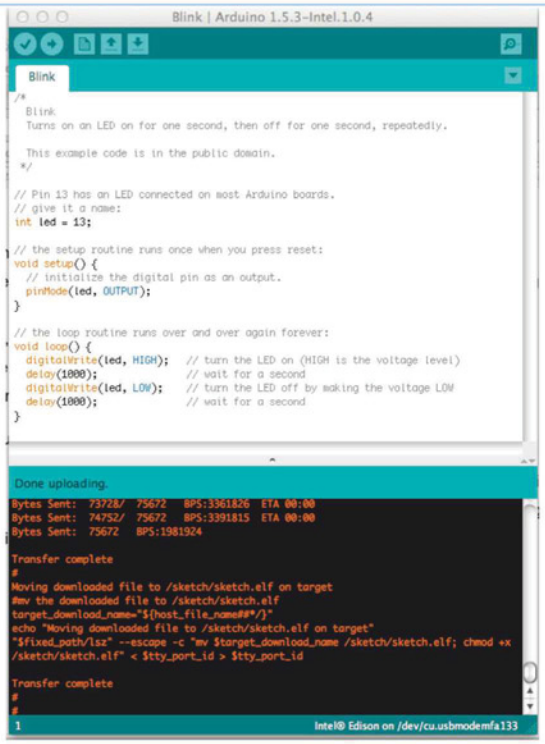

Figure 4: Uploading the Blink sketch to Intel Edison

Figure 3 shows the welcome screen that pops up when the cursor hovers over the Intel Edison's IP address. Future command line instructions can then be made via ssh and logging on to the Edison's root account.

The Intel Edison Arduino IDE should be downloaded from the Intel Maker site and installed on your computer. 'The Edison Getting Started Guide' recommends trying the supplied 'Blink' example sketch to verify that everything works correctly; the debug results will be seen as sketch transfers (see Figure 4).

Note the device address at the bottom right; this should match with the port you use when applying the 'screen' utility. Once uploaded, the small green LED to the right of the Edison module will blink.

Discovering IoT Features

With a working Intel Edison board, it is now time to uncover some of the extremely straightforward IoT features this platform offers. The necessary IoT tools, drivers and utilities are already pre-loaded so the board is ready to go. First, however, we need to set up an account on the cloud-based Intel analytics dashboard so our Edison can share sensor data with. Intel provides this dashboard for non-commercial applications; it is a very easy yet comprehensive platform which helps validate the design.

Within the dashboard there is a simple hierarchy of user account, devices and components. You can set up an account for a multiple number of edge node devices, such as individual Intel Edison modules (see Figure 5). Each node device needs to be authenticated to the analytics account it will report to, using a time-limited activation code. Each device can have a number of individual components, and by default these include temperature and humidity sensors and a power switch. Additional components can be added and assigned to each individual device, but each sensor must be registered with the analytics dashboard so that it can then record and chart the data received.

Managing Intel Edison connectivity to the analytics dashboard uses the iotkit-admin command. To check Edison can reach the cloud server, use the iotkit-admin test command.

Having set up an account within the dashboard and noted the activation code, the Edison device must be activated within one hour. Assuming the Edison has an Internet connection, it can be attached to the device via ssh and activated by entering the command iotkit-admin activation code, as shown in Figure 6.

Next, you'll need to register each attached sensor, which essentially means an alias to pass data.

At this stage in our example we don't yet have a temperature sensor attached to the Edison, but we can still register that temperature data will be coming from it, which can also be done from the command line during testing.

To register the temperature sensor, use the Edison command iotkit-admin register temp temperature.v1.0.

In this example 'temp' is all we need to identify the sensor when passing data to the cloud platform, and 'temperature.v1.0' denotes the component type and measurement attributes of this component as recorded in the account's catalogue section.

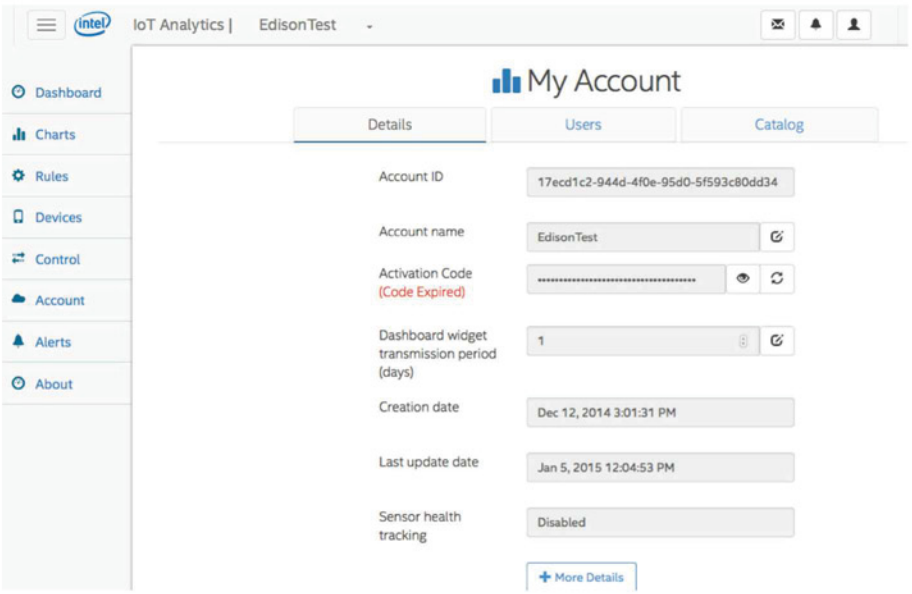

Figure 5: Intel IoT analytics dashboard

Sensor data or an 'observation' can be manually sent to the dashboard at any stage using the command:

iotkit-admin observation temp 24

Here 'temp' is the sensor component alias name and '24' is the temperature value you wish to send. Refresh your analytics dashboard and you should see the data start to appear.

Edison's Talking

Now we have a functioning Intel Edison talking to the cloud analytics dashboard, but how to automate sending data?

Thankfully, Intel provides example applications in both C/C++ and Node.js to make this process straightforward. Python is also supported with examples of all languages on the Intel communities' portal. Also, a set of IoT libraries (iotkit.h, aJSON.h, together with the standard Arduino Ethernet.h library) is provided for use with Arduino sketches, making it extremely easy to get an application running. For example, Figure 7 illustrates a simple temperature measurement sketch. A centigrade voltage-calibrated TMP36 temperature sensor from Analog Devices is connected between +5VDC and GND pins on the Arduino header with the centre output pin connected to the A0 (ADC input) pin.

The Intel Edison board opens up many opportunities to fast-track IoT design. Once the sensor I/O requirements have been decided and prototyped, a simple I/O board can be designed to match the Edison module and interface connectivity to a wide variety of attached sensors.

```
root@myEdison9:~# iotkit-admin activate XAWw9KNK
2014-12-22T14:58:47.788Z - info: Activating ...
2014-12-22T14:58:49.866Z - info: Saving device token...
2014-12-22T14:58:49.879Z - info: Sending attributes...
root@myEdison9:~#
```

Figure 6: Activation of Intel Edison to the Intel analytics dashboard

Figure 7: Arduino sketch of a simple IoT temperature sensor application

OLSON®

POWER DISTRIBUTION UNITS

WITH LOCAL AND REMOTE POWER MONITORING

FOR DATA CENTRE 19" RACKS VERTICALLY MOUNTED WITH COMBINATION IEC 320 C13 AND IEC 320 C19 24-36 SOCKETS 230V 16AMP - 32AMP SINGLE PHASE

Since 1961 OLSON have specialised in the manufacture of mains distribution panels and is an established supplier to many leading UK Companies.

All OLSON units are manufactured to ISO9001 and with our quality management systems existing in all parts of our organisation, you can expect the very highest standard of service from first contact through to the despatch of each order.

CALL OUR SALES HOTLINE

020 8905 7273

Made in the UK

OLSON® ELECTRONICS LIMITED

OLSON HOUSE, 490 HONEYPOT LANE, STANMORE, MIDDX HA7 1JY
TEL: 020 8905 7273 FAX: 020 8952 1232
e-mail: sales@olson.co.uk web site: http://www.olson.co.uk

MICROLEASE WILL DISTRIBUTE VIAVI PRODUCTS IN THE UK AND GERMANY

Microlease signed an agreement with the newly-formed Viavi Solutions (formerly JDSU) as its premier solutions partner in the UK and Germany. Microlease will sell test solutions from Viavi, complementing the rental and high-quality used equipment that Microlease already provides to these markets.

Viavi's advanced test solutions facilitate the deployment and optimisation of next generation communications network infrastructure and services. The $950m company was formed in August this year, by splitting JDSU into two groups: Lumentum and Viavi Solutions, each with a slightly different focus.

Viavi believes that as a result of its collaboration with Microlease it will be better positioned to tend to the needs of its customers and satisfy their specific sourcing requests.

www.microlease.com

AWS ELECTRONICS INTEGRATES QUOTING, ERP AND MANUFACTURING PROCESSES

AWS Electronics Group, one of Europe's leading specialist electronics manufacturing services providers, has invested in latest tools to provide seemless integration between quoting, ERP and manufacturing process data preparation. The BOM Connector software, provided by Router Solutions of Germany, forms a vital part of AWS's ongoing strategic investment program, linking recent investments in ERP (Infor Visual 8 Multi Site) and Process Preparation software (Valor).

BOM Connector applies intelligence to customers' BOM handling, linking parts and multiple approvals to ERP part numbers, resulting in a significant reduction in quote times where customers use common internal part libraries. It also generates RFQs and reads them back into the costings process, taking into consideration quality requirements and a pricing-based model. BOM and CAD data is compared, highlighting any inconsistencies, such as quantity or footprint errors.

www.awselectronicsgroup.com

MOUSER NOW STOCKS TE CONNECTIVITY'S CONNECTORS AND CABLE ASSEMBLIES

Mouser Electronics is now stocking TE Connectivity's (TE) micro SFP+ connector and cable assemblies, which offer footprints up to 50% smaller than current SFP+ interconnects. In addition, these products' designs have been enhanced to improve signal routing, minimize electromagnetic interference (EMI) and optimize automated manufacturing processes.

The 22-position connector supports data rates up to 10Gbps and withstands high-temperature pin-in-paste soldering up to 265 degrees Celsius. The integrated connector and cage with solder tail is designed for one-step board placement; the AWG 26 cable features a 360-degree braid crimp and an extended shield to minimize EMI.

TE's micro SFP+ connector and cable assemblies are electrically compliant to SFF-8431 and support a number of protocols including 10 Gigabit Ethernet, Gigabit Ethernet and Fibre Channel over Ethernet (FCoE).

www.mouser.com

FAST TRACK ETHERNET SWITCHES FEATURE PRECISION TIME PROTOCOL

Harting has expanded its range of Fast Track Ethernet switches for industrial applications with the FTS 3000-PTP range of managed switches.

The new devices feature Precision Time Protocol (PTP), allowing the creation of high-precision industrial networks in which all components of the automation process can be synchronised for time-critical applications.

The FTS 3000-PTP managed Ethernet switches support PTP in accordance with IEEE 1588v2 and can detect automation frames and accelerate them so that they always arrive at the destination in time, independent of the network load. Besides the Rapid Spanning Tree Protocol (RSTP), the switches support the Media Redundancy Protocol (MRP) for ring wiring and can be installed in various topologies. As a result, switch availability is boosted and system downtime is reduced.

www.harting.co.uk

SYNCHRONOUS BUCK REGULATOR IC WITH 3A OUTPUT AND WIDE INPUT VOLTAGE RANGE

The new A8654 from Allegro MicroSystems Europe is a high-output current synchronous buck regulator IC that can produce a 3A steady-state load current from an input voltage ranging from 4-36V.

The new device integrates low "on" resistance high-side MOSFETs and low-side n-channel MOSFETs, and utilizes external compensation to accommodate a wide range of power components. It uses pulse-width modulation (PWM) current mode control to provide simple compensation, excellent loop stability and fast transient response.

The A8654 remains operational even when the input drops as low as 2.6V. When the input voltage approaches the output voltage, the duty cycle is maximised to maintain the output voltage.

Other key features include externally set soft-start time, an external compensation network for power-train optimisation and others.

www.allegromicro.com

USB TYPE-C POWER DELIVERY CONTROLLER IC

Rohm has recently announced the development of a new class of power receiver controller ICs compatible with the latest USB Power Delivery (Rev2.0) and Type-C (Rev1.1) standards. The BM92TxxMWV series supports not only conventional USB power supply up to 7.5W, but the newly expanded power range as well up to 100W (20V/5A) for USB Type-C connected devices. This will make it possible to drive equipment with larger power requirements such as TVs and PCs via USB and at the same time enable conventional USB-equipped portable devices (i.e. smart phones, tablets) to be charged up to 4 times faster than the previous standard.

The new Type-C connector boasts a smaller, reversible, flippable cable design; USB PD offers scalable power using multiple power delivery modes.

www.rohm.com/eu

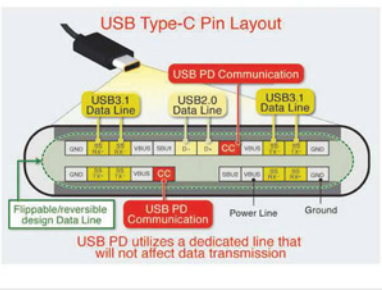

ENHANCED VERSION OF THE WORLD'S BEST-SELLING POWER METER

Yokogawa has introduced an enhanced version of its best-selling WT300 Series of compact, fifth-generation digital power meters, featuring higher accuracy, new measurement functionality and improved connectivity, including Modbus/TCP capability to aid integration into production environments.

The new series has a basic power accuracy of ±0.15% at 50/60Hz on all measurement ranges, along with a bandwidth of DC and 0.1Hz to 100kHz. The influence of power factor is also greatly reduced: at low power factor the accuracy is twice that of the previous models (±0.1% of apparent power S).

The WT300E series covers a broad range of input currents from a few milliamps to 40A RMS, making it equally suitable for measuring low currents in standby power testing to the high currents encountered in induction cookers.

tmi.yokogawa.com

TI'S LDC1101 1.8V INDUCTANCE-TO-DIGITAL CONVERTER, NOW AT MOUSER

Mouser Electronics is now stocking the LDC1101 inductance-to-digital converter (LDC) from Texas Instruments (TI). This a 1.8V to 3.3V, high-resolution data converter designed for short-range, high-speed, contactless sensing of position, rotation or motion. It provides accurate measurements in both controlled and harsh environments, making it ideal for automotive, consumer, industrial, computer and communications applications.

The LDC1101 features dual inductive measurement cores, allowing for > 150ksps 16-bit RP and L measurements. This can be done simultaneously with a high-resolution L measurement which can sample at > 180ksps with a resolution of up to 24 bits. The LDC1101 includes a threshold-compare function that can be dynamically updated while the device is running.

The supply current has a 1.4µA shutdown mode, 135µA sleep mode and 1.9mA active mode (no sensor connected).

www.mouser.com

HARWIN EXPANDS 1.27MM PITCH CONNECTOR FAMILY WITH NEW IDC PARTS

Harwin has expanded its popular 1.27mm pitch Archer M50 portfolio with the addition of new IDC connectors. The Archer family is distinguished in four ways: price, availability, reliability and high quality.

The new dual-row Archer connectors that have been added to the existing IDC range are 12-, 14- and 16-position connectors. Configurations include PCB-mounted ejector headers in both through-hole and SMT format, male IDC DIP transition-style and female IDC socket connectors for use with ribbon cable. Surface mount devices are packaged on tape and reel for easy auto placement.

The Archer connectors have been designed to facilitate easy, cost-effective connection between PCBs where significant quantities of interconnects are required, combined with a secure, quick connection method. Applications are found in many markets.

www.harwin.co.uk

RUGGED IP65 DOOR ENCLOSURES NEED NO HIDDEN EXTRAS

Hylec-APL, specialist supplier of electrical components, enclosures and rack systems, has extended its DE range of IP65 door enclosures – rugged, maintenance-free and cost-effective protection for long-life applications.

All DE door enclosures are supplied with a galvanised steel back plate, external mounting brackets and a lock and key as standard, so there are no hidden costs. Made from flame-retardant ABS, the enclosures feature wall thicknesses of up to 3.5mm to offer impact resistance of IK08 (protection against impacts with an energy up to 5J).

Because ABS is non-corrosive, the enclosures deliver protection from continued exposure to external conditions, even in marine applications. Liquid gasket seals ensure IP65 protection is maintained, even when the doors are repeatedly opened and closed for regular access.

www.hylec-apl.com

WORLD'S FIRST SUPERMHL SOLUTIONS FROM LATTICE

Lattice Semiconductor announced the world's first superMHL products for USB Type-C to deliver 4K 60fps RGB/4:4:4 video with concurrent USB 3.1 Gen 1 or Gen 2 data. The Sil8630 and Sil9396 are a low-power superMHL transmitter and receiver pair that can deliver and receive 4K 60fps over a single lane, enabling a PC experience with USB Type-C devices.

The Sil8630 transmitter is able to seamlessly interface with HDMI 2.0 transmitters already integrated into the application processors used in the latest phones, tablets and notebooks.

The Sil9396 receiver is ideal for MHL adapters and docks. When paired with the Sil7023 or Sil7033, MHL accessories can be designed to connect USB Type-C mobile and PC products to HDMI displays and USB devices such as keyboards, mice and external storage.

www.lattice.com

THE MOLEX MINI50 UNSEALED CONNECTOR SYSTEM NOW AT TTI

The new Molex Mini50 unsealed connector system is now available in Europe at TTI, Inc.

Designed to meet the demand for smaller interconnects from car manufacturers, the Molex Mini50 has smaller terminals to fit more signals into vehicle interiors and delivers 50% space savings over traditional USCAR 0.64mm connectors. It is approved as the industry's only USCAR 050 interface.

The integration of multiple devices in today's transportation industry requires harnesses that are lighter, smaller and more cost-effective. Molex Mini50 harnesses deliver highly reliable performance in limited spaces, and are suitable for infotainment, lighting and HVAC system applications.

The Molex Mini50 unsealed connector system includes 4, 8, 12, 16, 20 and 24 circuit size receptacles and headers in single row and dual row configurations.

www.ttieurope.com

ECOPAC UK POWER LTD

Enclosed
Power Supplies

Open Frame
Power Supplies

MEAN WELL

DIN Rail
Power Supplies

For Further Information:

Call: 01844 204420

Website: ecopacpower.co.uk

Email: sales@ecopacpower.co.uk

PROTEUS 8.3

ECAD to MCAD made easy

Data Exchange with STEP/IGES

AUTODESK. PTC

SOLIDWORKS

The Proteus Design Suite now includes full support for data exchange with Mechanical CAD packages via the STEP/IGES file formats. This allows you to better visualise your design and helps quickly solve fixtures, fittings and casement problems.

Import 3D STEP/IGES models for your parts and visualise inside the Proteus Design Suite. Export your completed board to Solidworks or other MCAD software.

Visit www.labcenter.com

Tel:+44 01756753440 E-Mail info@labcenter.com

Labcenter Electronics Ltd, 21 Hardy Grange, BD23 5AJ

Labcenter Electronics www.labcenter.com

10 PORT & 20 PORT USB CHARGING & SYNC HUBS

Powersolve professional USB charging & sync hubs are ideal for schools, businesses or in fact any application requiring multiple connection to USB devices, for either charging or data transfer

PSUSB-10CH & PSUSB-20CH

Features

- Charges and syncs up to 10 devices (PSUSB-10CH), or 20 devices (PSUSB-20CH)
- Charge current 2A for 10 port hub and 1.1A for 20 port hub
- Supports high speed 480 Mbps, full speed 12 Mbps and low speed 1.5 Mbps operation
- Compatible with all USB compliant devices
- 10 or 20 USB 2.0 downstream ports, depending on model
- Over current detection and protection and surge and ESD protection
- 3 x 10 port devices can be connected in cascade to give up to an optimum of 30 USB ports
- 2 x 20 port devices can be connected in cascade to give up to an optimum of 40 USB ports
- Supports Windows 98SE/ME/2000/XP/Vista/7/8/ and Mac OS 8.6/9.X/10.X and higher

10 Ports 60 & 120 Watts USB Charger (charging only)

PLV120-USB

Features

- Universal 90-264VAC Input
- IEC320 C8 2 pin AC Input Connector (UK power cord included)
- Output ports, 10 x 5V 2.4A
- Will charge any device powered by standard USB charging technology, with smart charging IC
- EMC to EN55022'B', CISPR22 'B' & FCC 'B'
- Full International Safety Approvals & CE marked
- Compact Desk Top Enclosure with On/Off switch
- Meets ROHS requirements

Features

- Universal 90-264VAC Input
- IEC320 C8 2 pin AC Input Connector (UK power cord included)
- Outputs switchable from 10 x 5V 1A or 5 x 5V 2.4A
- Will charge most devices powered by standard USB 5VDC chargers
- EMC to EN55022'B', CISPR22 'B' & FCC 'B'
- Full International Safety Approvals & CE marked
- Compact Desk Top Enclosure
- Meets ROHS requirements

PLV60-USB

POWER SOLVE

www.powersolve.co.uk

Tel: 44-1635-521858 Email: sales@powersolve.co.uk